



Low-order representations of the canonical wind turbine array boundary layer via double proper orthogonal decomposition

Nicholas Hamilton, Murat Tutkun, and Raúl Bayoán Cal

Citation: Physics of Fluids **28**, 025103 (2016); doi: 10.1063/1.4940659

View online: <http://dx.doi.org/10.1063/1.4940659>

View Table of Contents: <http://scitation.aip.org/content/aip/journal/pof2/28/2?ver=pdfcov>

Published by the AIP Publishing

Articles you may be interested in

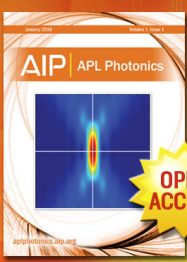
The effects of mean atmospheric forcings of the stable atmospheric boundary layer on wind turbine wake
J. Renewable Sustainable Energy **7**, 013124 (2015); 10.1063/1.4907687

Identification of Markov process within a wind turbine array boundary layer
J. Renewable Sustainable Energy **6**, 023121 (2014); 10.1063/1.4869566

Streamwise development of the wind turbine boundary layer over a model wind turbine array
Phys. Fluids **25**, 085108 (2013); 10.1063/1.4818451

Large eddy simulation study of scalar transport in fully developed wind-turbine array boundary layers
Phys. Fluids **23**, 126603 (2011); 10.1063/1.3663376

Large-eddy simulation of a very large wind farm in a stable atmospheric boundary layer
Phys. Fluids **23**, 065101 (2011); 10.1063/1.3589857



Launching in 2016!
The future of applied photonics research is here

AIP | APL
Photonics

Low-order representations of the canonical wind turbine array boundary layer via double proper orthogonal decomposition

Nicholas Hamilton,¹ Murat Tutkun,^{2,3} and Raúl Bayoán Cal¹

¹*Department of Mechanical and Materials Engineering, Portland State University, Portland, Oregon 97202, USA*

²*Department of Process and Fluid Flow Technology, IFE, 2007 Kjeller, Norway*

³*Department of Mathematics, University of Oslo, Blindern, 0316 Oslo, Norway*

(Received 8 September 2015; accepted 11 January 2016; published online 5 February 2016)

Wind turbine wakes are investigated in order to characterize the development of energetic turbulence structures. Experimental data from stereo particle image velocimetry render the full Reynolds stress tensor accessible in planes parallel to the swept area of the scale model turbine rotor. Proper orthogonal decomposition (POD) is applied to decompose and analyze structures in the wake. The modes resulting from the decomposition demonstrate that structures grow and develop along the streamwise direction. A second iteration of the snapshot POD, otherwise called double proper orthogonal decomposition (DPOD), is applied to modes of common rank from the span of measurement locations yielding an ordered set of projections. The DPOD describes the sub-modal organization in terms of largest common projection and a series of correction modes with coefficients that are functions of the streamwise coordinate. Sub-structures of POD modes that persist through the wake have a dominant projection that accounts for the character of individual POD modes. Distribution of eigenvalues associated with DPOD modes indicates that near-wake turbulence behavior is superimposed on overall wake structure. High order POD modes do not reveal any common projections in the measurement sets of the wake and associated eigenvalues are nearly equal. The eigenvalues from the DPOD indicate that the structure of the wind turbine wake can be described with a small subset of the original mode basis. The truncated basis of sub-modal structures represents a total reduction to 0.015% of the degrees of freedom of the wind turbine wake. Low-order representations of the Reynolds stress tensor are made for the wake using the most dominant DPOD modes. The stress tensor is corrected to account for energy excluded from the truncated basis. A tensor of constant coefficients is defined to rescale the low-order representation of the stresses to match the original statistics. That a constant correction for each term in the Reynolds stress tensor is sufficient to correct the wake suggests that high order modes account for a nearly constant, isotropic turbulence kinetic energy. The following method reconstructs diagonal elements of the stress tensor to a root-mean-square error within 15% and shear terms to within 3%. © 2016 AIP Publishing LLC.
[<http://dx.doi.org/10.1063/1.4940659>]

I. INTRODUCTION

The turbulent flow in a wind turbine array (WTA) canopy combines the atmospheric boundary layer, wake-to-wake interaction, and fluid/structure interactions. Wind turbine wakes are asymmetrical, subject to large changes in flow conditions and, in large arrays, subject to wake-to-wake interactions. As such, wind turbine wakes represent a complex flow to quantify and describe. Given the observed under-performance of turbines in large arrays, the characterization wind turbine wakes is an important subject for diagnosis and optimization. The rapid pace at which wind energy is being adopted to meet global energy needs further underpins the need for specific research in this area.

A WTA is considered to have met the “fully developed” condition when flow statistics in the wake exhibit periodicity from row to row,⁵ generally considered a good approximation beyond the fourth row of turbines in a Cartesian WTA arrangement. Wake flow statistics beyond the fourth row of turbines are assumed to approximate successive rows in the array.^{4,5,7,20} For large WTAs, the kinetic energy ultimately extracted by turbines must be transported from above the array to the canopy layer.^{3,4,11} The resupply of mean flow kinetic energy to flow where one observes momentum-deficit is largely accomplished by turbulence. The shear layer at the border of each wake exhibits strong gradients in mean velocities and significant turbulence shear stresses. Other experimentation in wind farms has shown that the flux of kinetic energy is mainly expressed by the energetic turbulent structures. Large-scale dominance of energy fluxes was shown by way of the premultiplied spectral density¹¹ and the proper orthogonal decomposition.¹³

The proper orthogonal decomposition (POD) was introduced to the study of turbulence by Lumley¹⁹ and later modified by Sirovich²⁶ to apply to data that have fine spatial resolution but poor temporal resolution. The snapshot POD has been applied to wind turbine wakes by Hamilton *et al.*¹³ wherein large structures were identified as being responsible for most of the flux of kinetic energy. The study showed that relatively few modes were needed to account for the majority of the turbulence kinetic energy, k , in the wake of a wind turbine. The POD has also been applied to data resulting from LES simulations of an infinite turbine array by VerHulst and Meneveau,²⁹ confirming that there are very large structures on the order of spacing of devices in the array that have an influence on global performance. Large-scale structures in a wind farm were reproduced from LES data using the POD by Sørensen *et al.*,²⁷ where it was shown that selected POD modes relate spatial development of the wake. Lignarolo *et al.*¹⁸ used snapshot POD to filter data and distinguish tip vortices shed by wind turbine rotors from the background turbulence. Another recent study² combined the snapshot POD with preprocessing of PIV images to distinguish turbulent features in the wake from those arising from the atmospheric boundary layer.

A modified version of the POD models, proposed by Noack *et al.*,²¹ allowed for variation in the mean flow. Relatively recent methodological development with the proper orthogonal decomposition includes iterative application of POD to similar sets of data. Siegel *et al.*²⁵ showed that POD bases of identical size for multiple datasets in a flow may exhibit variation according to mode number following the nature of the flow, in that case a cylinder wake with vortex shedding. The work identified that modes of like rank exhibit subtle differences between periods of a cylinder wake. Variability between modes of common rank was characterized through the secondary application of the POD referred to simply as the double POD (DPOD). The span of like modes was characterized by a large common projection and a set of corrections termed “shift” modes, whose significance is described by their respective coefficients. Spatial variations in POD modes are accounted for during the oscillation cycle and during the application of external forcing.

The optimality of the POD in describing the energy of a flow provides a direct means of filtering velocity measurements.¹⁴ The reconstruction of a velocity signal may be accomplished using a truncated set of POD modes in linear combination. Filtering in this manner typically follows establishing a threshold of turbulence kinetic energy according to the eigenvalues associated with each POD mode. Additionally, the eigenvalue decomposition sorts random and incoherent noise to higher mode numbers and are typically excluded in reduced order representations.⁹ The kernel of the POD is most commonly the two-point spatial correlation tensor and may be reconstructed directly from the POD modes and associated eigenvalues. With a reduced order model of this sort, individual velocity snapshots neither are necessary beyond the initial decomposition nor are they produced by the model.

Reconstruction using a reduced basis necessarily excludes energy from the flow. Excluded energy is associated with smaller-scale turbulent scales or ones that are not coherent in time, regardless of their potential dynamical importance.^{15,28} Often statistics produced with reduced order models are structurally representative of the full flow, but exhibit a decreased range of magnitudes due to the exclusion of turbulence kinetic energy in intermediate and high mode numbers.¹³

The following work constitutes a wind tunnel experiment of a scaled WTA with a particular focus on the turbulent wake deep in the array. Turbulence structures in the wakes of wind turbines are shown to evolve spatially, demonstrated by the mode coefficients of the DPOD. Measurements of the wake are decomposed and simplified to provide accurate descriptions of the statistics with

severely reduced degrees of freedom. It is shown that the low-order descriptions may be corrected by introducing a set of coefficients to compensate for the truncated modal bases. The accuracy of low-order reconstructions is quantified and indicates a good agreement with the original statistics. The resulting description has the potential to augment existing wind turbine array models with more complete representation of wake interaction and dynamics.

II. THEORY

The turbulent flow in the wind turbine array canopy layer is described by the mean kinetic energy equation simplified under conventional boundary layer assumptions,

$$U_j \frac{\partial \frac{1}{2} U_i^2}{\partial x_j} = -\frac{1}{\rho} U_i \frac{\partial P}{\partial x_i} + \overline{u_i u_j} \frac{\partial U_i}{\partial x_j} - \frac{\partial \overline{u_i u_j} U_i}{\partial x_j} - \mathcal{F}_i. \quad (1)$$

Capitalization of variables is employed to indicate ensemble averaged quantities, while lower-case letters refer to zero-centered fluctuations about the mean. Equation (1) has been simplified by omitting the unsteady term through ensemble averaging of the equations. A further simplification is made by considering only measurement locations sufficiently far from solid bodies such that viscous terms can be neglected when compared to inertial terms. A sink term is introduced to the equation in the form of thrust from the turbines acting primarily in the streamwise direction, \mathcal{F}_i . In the present development, coordinates are designated as x , y , and z for the streamwise, wall-normal, and spanwise directions, respectively. An overline signifies that an ensemble average of a product of two quantities has been taken. The left side of Equation (1) is the convective term and is balanced on the right side by four terms representing energy added to the flow through pressure gradients, the production of turbulence kinetic energy, the flux of mean flow kinetic energy by turbulence, and the energy removed from the flow by the action of a wind turbine rotor, respectively.

The turbulence field in a wind turbine wake is highly variable due to the complex nature of the flow, issuing from rotating bodies that periodically force the flow and create high-energy vortices. Wakes interact in a wind turbine array, frequently analogized as a canopy and are submerged in the atmospheric boundary layer. Due to the highly complicated nature of the flow, dynamics have eluded complete characterization. The flux and production of turbulence kinetic energy terms in Equation (1) play a significant role in the overall energy balance in the wake and in the wind turbine canopy. These terms rely on large-scale turbulent structures, which the proper orthogonal decomposition is optimally suited to identify.

A. Snapshot proper orthogonal decomposition

Snapshot POD as follows is in the vein of the original development by Sirovich²⁶ and is applied to flow data with high spatial resolution relative to temporal resolution. The outputs of the decomposition are an ordered set of modes and eigenvalues denoting the energy associated with each mode. The organized basis of modes from the POD has been described as projections common to the span of snapshots in a dataset.^{1,14,26}

In the following development, bold math symbols represent vectorial quantities and symbols in plain text are scalar quantities. The flow field is assumed to be a stochastic function of space and time. Velocity snapshots are then denoted as $\mathbf{u}(\mathbf{x}, t^n)$, where \mathbf{x} and t^n refer to the spatial coordinates and n th time sample, respectively. The spatial correlation tensor is defined as

$$\mathbf{R}(\mathbf{x}, \mathbf{x}') = \frac{1}{N} \sum_{n=1}^N \mathbf{u}(\mathbf{x}, t^n) \mathbf{u}'^T(\mathbf{x}', t^n), \quad (2)$$

where N signifies the number of snapshots and the prime represents the spatial coordinate of another point in the domain. The two-point spatial correlation tensor forms the kernel of the POD integral equation. It is assumed that a basis of N modes can be written in terms of the original data as

$$\Phi(\mathbf{x}) = \sum_{n=1}^N A(t^n) \mathbf{u}(\mathbf{x}, t^n), \quad (3)$$

where $\Phi(\mathbf{x})$ is a deterministic field that has the largest projection on the stochastic velocity field in a mean square sense. The velocity snapshots combine linearly with the time-dependent coefficients $A(t^n)$ to form the POD modes in Equation (3).

The POD integral equation is written,

$$\int_{\Omega} \mathbf{R}(\mathbf{x}, \mathbf{x}') \Phi(\mathbf{x}') d\mathbf{x}' = \lambda \Phi(\mathbf{x}), \quad (4)$$

where λ is the set of eigenvalues relating Φ to \mathbf{R} . Equations (2) and (3) are substituted into Equation (4) and discretized such that the integral equation, which takes the form of an eigenvalue problem, may be solved numerically in the following form:

$$\mathbf{C}\mathbf{A} = \lambda\mathbf{A}. \quad (5)$$

In Equation (5), \mathbf{A} is a vector of coefficients corresponding to each snapshot in time and \mathbf{C} is an approximation of the correlation tensor from Equation (2).

Solving Equation (5) yields the set of coefficients from which the POD modes are computed according to Equation (3). These modes are typically normalized with their own L^2 -norm to form an orthonormal basis,

$$\Phi^{(i)}(\mathbf{x}) = \frac{\sum_{n=1}^N A^i(t^n) \mathbf{u}(\mathbf{x}, t^n)}{\|\sum_{n=1}^N A^i(t^n) \mathbf{u}(\mathbf{x}, t^n)\|}, \quad i = 1, \dots, N. \quad (6)$$

Stochastic velocity fields may then be reconstructed using the eigenfunctions of the POD,

$$\mathbf{u}(\mathbf{x}, t^n) = \sum_{i=1}^N a_i \Phi^{(i)}(\mathbf{x}), \quad (7)$$

where a_i is a set of coefficients obtained by back-projecting the set of stochastic velocity fields onto the POD modes,

$$a_i = \int_{\Omega} \mathbf{u}(\mathbf{x}, t^n) \Phi^{(i)}(\mathbf{x}) d\mathbf{x}. \quad (8)$$

Using a truncated set of POD modes results in a filtered turbulent flow field according to the turbulence kinetic energy associated with each mode.

The POD provides the optimal set of eigenfunctions that decompose the turbulence in a mean-squared sense into functions and eigenvalues representative of the energy. Fluctuating velocity measurements are reconstructed as in Equation (7) and, by extension, the Reynolds stress tensor may be reconstructed directly from the POD modes according to

$$\overline{\mathbf{u}_i(\mathbf{x}) \mathbf{u}_j(\mathbf{x})} = \sum_{n=1}^N \lambda^{(n)} \phi_i^{(n)}(\mathbf{x}) \phi_j^{(n)}(\mathbf{x}). \quad (9)$$

Reconstructed Reynolds stresses in Equation (9) are used to study quantities in the transport equation for the mean kinetic energy. The POD may be used as a means of order reduction either by Equation (7) to reconstruct velocity snapshots filtered by truncated POD bases or by Equation (9) in which the kernel is reconstructed directly. Statistics based on the reconstructed data using a truncated set of POD modes will be denoted in the following text with an over-ring and a subscript indicating the number of POD modes (N_r) or percent of the total energy used in reconstruction as $\overline{\dot{\mathbf{u}}\dot{\mathbf{v}}}|_{N_r} = \sum_{n=1}^{N_r} \lambda^{(n)} \phi_u^{(n)} \phi_v^{(n)}$ or, following Equation (7), $\dot{\mathbf{u}}|_{N_r} = \sum_{n=1}^{N_r} a_n \Phi^{(n)}$.

B. Double POD

The snapshot POD outlined above is applied to dataset from each measurement location individually. The spatial development of turbulence structures in the wake is shown along the streamwise

coordinate x . As each measurement set contains the same number of snapshots and therefore the same number of POD modes, it is safe to assume that the ordering of structures in the POD basis is similarly organized.^{23–25} The development of $\Phi^{(n)}(x)$ in the wake is characterized by the linear combination of sub-modal structures and corresponding coefficients. With increasing mode number n , structural organization is lost in each set and fails to communicate development downstream. Energetic features as indicated by low mode numbers show correspondence between the measurement sets throughout the wake and are seen to evolve spatially with x .

Applying the POD to sets of modes of common rank, that is modes at a fixed mode number n from each separate POD basis, then shows the sub-modal structures, previously termed “shift modes.” With such an application of DPOD the internal basis of POD modes is already time independent (dependence on time is now accounted for by the series of mode coefficients a_n) and the DPOD accounts for cycle-to-cycle differences in bases. In the current formulation of the DPOD, decomposition occurs over the streamwise coordinate designated by x^m , where m refers to the spatial location of each measurement set. An analog was used in the original POD to differentiate snapshots in time as t^n . Concatenating modes of common rank formulate new sets of snapshots as $\Phi^{(n)}(x^m)$. The difference between the POD and the DPOD two lies in definition of the kernel, which is now a correlation between POD modes at fixed mode number $D^n(x^m)$ organized in space, rather than velocity snapshots organized in time

$$D^n(x^m) = \frac{1}{M} \sum_{m=1}^M \Phi^{(n),T}(x^m) \Phi^{(n)}(x^m), \quad (10)$$

where index n refers to the POD bases by mode number, index m now refers to snapshots arranged according to the streamwise coordinate x , and M is the number of snapshots (POD modes) used to form the kernel. DPOD is applied iteratively to sets of $D^n(x^m)$, increasing mode number n with each iteration.

The eigenvalue problem is now written,

$$D^n B^n = \Lambda^{(n,m)} B^n. \quad (11)$$

DPOD modes can be expressed in a form analogous to the previous formulation,

$$\Gamma^{(n,j)} = \frac{\sum_{j=1}^M B^j(x^m) \Phi^{(n)}(x^m)}{\|\sum_{j=1}^M B^j(x^m) \Phi^{(n)}(x^m)\|}, \quad j = 1, \dots, M. \quad (12)$$

Streamwise dependence of modes has been removed through the DPOD in the same sense that temporal dependence was removed through the POD. The DPOD modes $\Gamma^{(n,j)}$ are the span of j sub-modes of each of the original n POD modes.

As with snapshot POD, the span of eigenvalues of the DPOD describes the significance of each of the sub-modes in the vectorial space of the POD modes. Eigenvalues $\Lambda^{(n,m)}$ are a matrix with dimensions that match the original number of snapshots (n) at each measurement location and the number of sub-modes (m , corresponding to the number of measurement planes).

Analogous to the initial decomposition $\Phi^{(n)}$ may be reconstructed using the sub-modal structures from the DPOD,

$$\Phi^{(n)}(x^m) = \sum_{j=1}^M b_{n,j} \Gamma^{(n,j)}, \quad (13)$$

where $b_{n,j}$ are the coefficients of the sub-modes obtained by back-projecting the set of Φ onto Γ ,

$$b_{n,j} = \int_{\Omega} \Phi^{(n)}(x^m) \Gamma^{(n,j)} d\Omega. \quad (14)$$

The coefficients $b_{n,j}$ communicate the spatial organization and significance of each sub-mode whereas the sub-modes themselves $\Gamma^{(n,j)}$ are independent of x . In reconstructing POD modes from sub-modal structures, the dependence of $\Phi^{(n)}$ on x is contained in the sub-modal coefficients.

In making reconstructions via DPOD, the cross correlation of POD modes is not the goal, but rather a series of filtered modes. Equation (13) can be used to develop $\hat{\Phi}^{(n)}|_{M_r} = \sum_{m=1}^{M_r} b_{n,m} \Gamma^{(n,m)}$, where M_r is the number of sub-modes in the truncated set. Note that the over-ring is still used to indicate that a quantity has been filtered, even at the sub-modal level. Stresses are then reconstructed with a truncated set of filtered POD modes as $\bar{uv}|_{N_r}^{M_r} = \sum_{n=1}^{N_r} \lambda^{(n)} \hat{\phi}_u^{(n)} \hat{\phi}_v^{(n)} |_{M_r}$. The number of sub-modes used in filtered POD modes is designated by M_r .

Double POD as proposed here may be applied to any collection of related POD modes. If there exists no common projection between the elements of the kernel, the DPOD will provide no appreciable organization of sub-modal structures. The method is appropriate for any type of turbulent flow (wake, jet, developing boundary layer, etc.), provided that the POD bases being concatenated for further decomposition are interrelated. Analogous to the snapshot POD over time, the kernel of the DPOD need not be formed of POD modes resulting from measurements at regularly spaced locations. The series of reconstruction coefficients $b_{n,m}$ weights the sub-modes according to their original spatial distribution. If POD modes forming the kernel are regularly spaced, sub-modal coefficients form uniform series in space. Contrarily, if the kernel is formed from randomly spaced POD modes, $b_{n,m}$ will not yield well-organized spatial dependence of the sub-modes.

The procedure followed in the current work is illustrated in Figure 1. Each stage of the analysis is designated with a letter from (A) to (E). The figure denotes snapshot sets as long boxes and modes as pegs with heights that vary to convey their relative importance in each modal basis. Horizontal alignment is representative of the organization of snapshots in time. The streamwise coordinate is shown moving back through the figure. The initial application of the POD from (A) to (B) results in a basis of 2000 POD modes at each measurement location that are not themselves dependent on time. The temporal dependence of each dataset is accounted for in the series of mode coefficients a_n , not

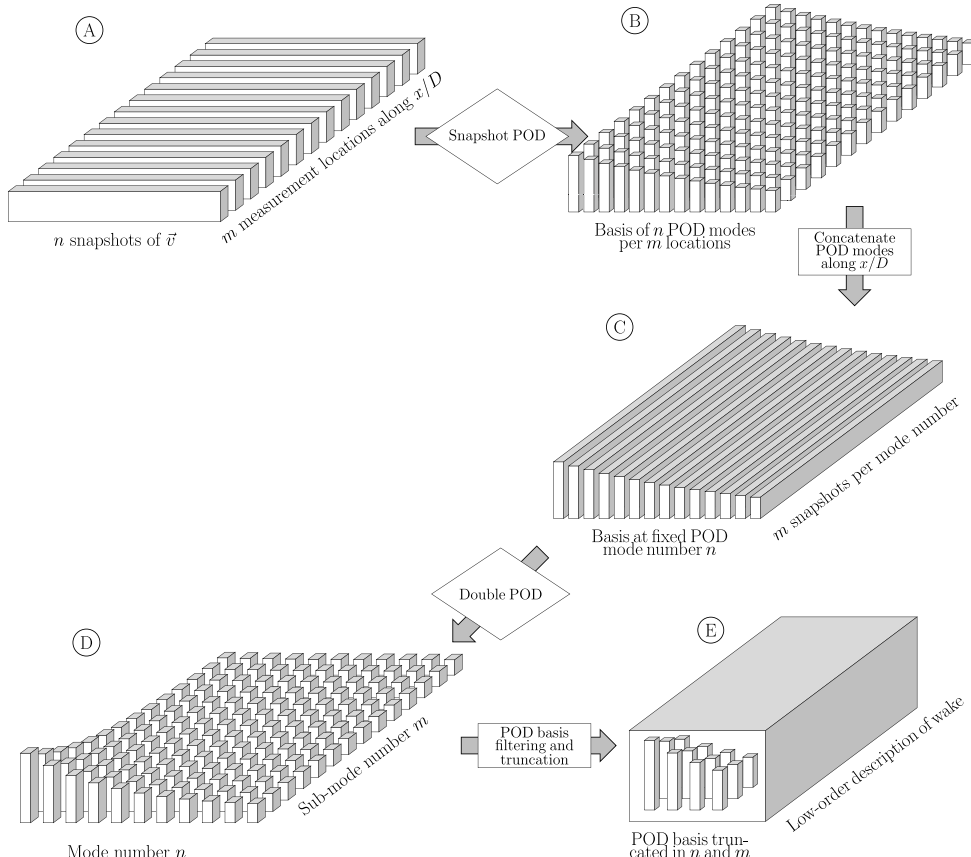


FIG. 1. Conceptual diagram showing the analysis procedure from velocity snapshots through applications of the POD and formation of a low-order description of the turbulent wind turbine wake.

shown in the diagram. The independence of $\Phi^{(n)}$ from time is signified by the separation of the basis into elements. Concatenating the POD modes along the streamwise coordinate yields new snapshot sets organized spatially rather than temporally (C).

In a similar sense, the application of the DPOD (from (C) to (D)) displaces the dependence of the POD modes on the streamwise coordinate to the sub-modal coefficients $b_{n,m}$. After secondary decomposition, the separated elements in stage D are representative of sub-modal structures. The first sub-mode is the largest common projection of fixed POD mode number throughout the wake, an effective average mode immune to the switching of the algebraic sign seen in individual POD bases. Truncating the DPOD basis amounts to filtering POD modes at the sub-modal level $\dot{\Phi}^{(n)}|_{M_r}$. Filtered modes are composed by linear combination of the largest common projection (effective average) and successively more nuanced corrections. Limiting the filtered POD basis is the formation of the low-order description of the wake discussed herein. The limited span of filtered POD modes $\dot{\Phi}^{(n)}|_{M_r}$ is used to represent the Reynolds stress tensor according to Equation (9). The selections of thresholds used in truncation are discussed in further detail in the following analysis.

III. EXPERIMENTAL SETUP

An array of wind turbines was constructed at model scale in the closed circuit wind tunnel facility at Portland State University. The wind tunnel features a 9:1 contraction ratio to eliminate effects were introduced by the powering fan and guide vanes in the corners. The cross section of the wind tunnel is constant with dimensions of $1.2\text{ m} \times 0.8\text{ m}$ (spanwise and vertical directions, respectively) throughout the length of the test section. The inlet of the test section was furnished with a passive grid composed of seven horizontal and six vertical rods to introduce large scale turbulence to the flow. Vertical stakes (0.0125 m thick plexiglass) shaped to precondition the boundary layer in the wind tunnel in order to increase the high-shear region of the flow near the wall. The stakes were spaced by 0.136 m across the width of the tunnel, 0.35 m downstream of the passive grid. Roughness was added to the inlet of the flow in the form of chains with average diameter of 7.5 mm . All surfaces of the test section have been constructed of schlieren-grade annealed float glass mounted to the framework of the tunnel to enable non-intrusive optical measurement techniques in multiple configurations. Further detail on the wind tunnel and the setup for wind turbine array experiments, including a characterization of the inflow to the model-scale wind farm, in Hamilton *et al.*¹²

The model-scale wind turbines (Figure 2) were fabricated in-house, designed to emulate a 1 MW horizontal-axis device commonly used in full scale wind energy projects. Model turbines have three blades with a pitch at the base of approximately $\gamma_{root} = 22^\circ$ and at the tip of approximately $\gamma_{tip} = 15^\circ$. The 7° twist from root to tip approximates the aerodynamics of wind turbine blades at the laboratory scale. The nacelle of each model turbine is composed of an electric motor (Faulhaber GMBH & Co., Series 1331T012SR). The motors are powered at the shaft and behave as generators. The operating point of each motor is controlled by a resistive load applied across the leads. Each model turbine was tuned to match the peak power coefficient according to studies made with the same models and wind tunnel.^{10,12,13} (Measurements of power and power coefficient are not discussed in the present work but can be found in Hamilton and Cal¹⁰ and Hamilton *et al.*¹²) The hub height of each turbine model was equal to the rotor diameter D .

Recent wind tunnel experiments consider a Cartesian array to be fully developed after the fourth streamwise row of devices, beyond which the statistics become quasi-periodic from row-to-row.^{5,6} In the experiment, wind turbines were arrayed to match established wind tunnel arrangements to aid in comparison with previous results.^{10–13} Figure 3 depicts geometry of the wind turbines in the model array relative to measurement planes. The spacing of model turbines was $6D \times 3D$ in the streamwise and spanwise directions, respectively (denoted as S_x and S_z). Spacing of the turbines is expected to amplify wake interaction and development of the wind turbine canopy layer.

Velocity measurements were undertaken with stereo particle image velocimetry (SPIV) in planes parallel to the swept area of the rotor. Figure 3 relates the measurement fields to the model array used in the wind tunnel. SPIV enables two dimensional, three component (2D-3C) measurements, in each plane accessing the full Reynolds stress tensor and in-plane gradients. Measurement planes

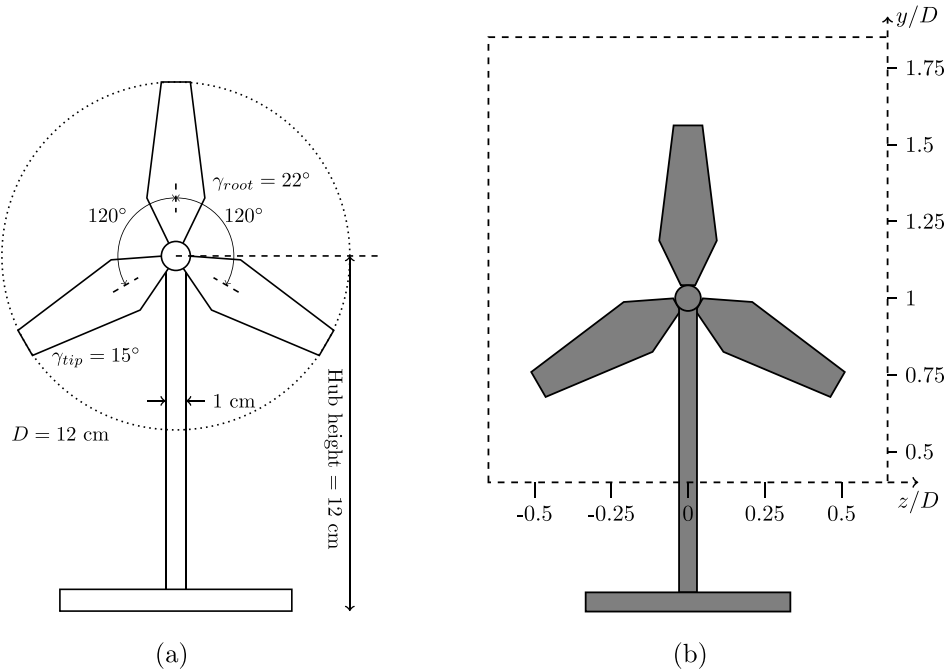


FIG. 2. Schematic of the model-scale wind turbines used in the wind turbine array, (a). Model is also shown relative to the SPIV measurement window in the wakes with affixed coordinate system, (b).

in the current experiment were oriented to resolve gradients across the wakes. A scaling argument can be made that gradients along the streamwise coordinate are expected to be smaller than those in the wall-normal and spanwise directions except immediately following the wind turbine ($x/D \leq 1$). Each SPIV measurement window was approximately $0.2 \text{ m} \times 0.25 \text{ m}$ in the spanwise and wall-normal directions, respectively. Snapshots were taken at a time delay of $\delta t = 180 \mu\text{s}$. The Nd:Yag (532 nm, 1200 mJ, 4 ns duration) double-pulsed laser sheet varied from 1 mm at the bottom of the tunnel to approximately 2 mm at the top of the measurement window.

The time delay and sheet thickness were optimized to minimize the out of plane loss of particle pairs while maximizing light intensity. The flow was periodically reseeded with vaporized di-ethyl-hexyl-sebacat and the concentration of the seeding was kept at a constant level to ensure consistency of particle imaging. Cameras (4MP ImagerProX) used to collect flow snapshots were arranged beneath the wind tunnel floor looking vertically upward in the general direction of the laser sheet, placing them in back-scatter. Cameras were approximately 45 cm apart arranged symmetrically around the

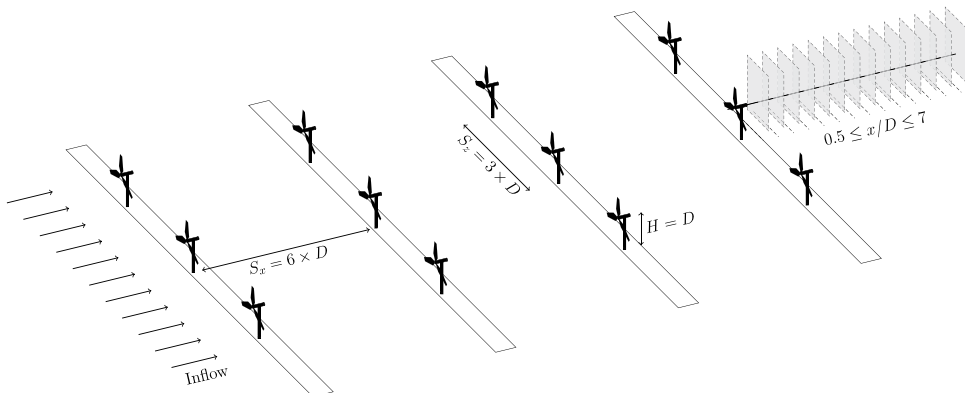


FIG. 3. Model-scale array used in the current experiment relating turbine spacing and measurement locations behind the fourth row.

streamwise coordinate. Velocity vectors were calculated using a multi-pass FFT based algorithm with two passes each at 64 and 32 pixel interrogation windows. The final spatial resolution of velocity vectors was approximately 1.4 mm in both the spanwise and wall-normal directions. Each streamwise location required an individual calibration to ensure accurate results. Each measurement set in x/D is composed of 2000 SPIV snapshots for converged statistics. Statistical error of second order quantities was calculated to be approximately 3%. Measurement error was calculated following the error analysis methodology described by Prasad.²²

IV. RESULTS

Flow statistics were calculated in each measurement plane, shown in Figure 4. The measurement plane located at $x/D = 3.5$ was corrupted by reflections that introduced noise to the mean statistics that intensified at higher order and has been excluded from the results below. Flow statistics are normalized by the incoming wind speed at hub height $U_{\text{hub}} = 4.75$ m/s. The mean streamwise velocity U shows the characteristic momentum deficit of the wake in Figure 4(a). As anticipated, the strongest momentum deficit is evident directly behind the nacelle of the wind turbine model at $x/D = 0.5$. Recovery of the wake is seen progressing throughout the wake as x/D increases. By $x/D = 5$, the mean streamwise velocity increases monotonically with y/D , confirming the results from previous studies.¹¹ Gradients of U across the wake are of equal order of magnitude in both the spanwise and wall-normal directions. As the wake recovers ($x/D \geq 4$), the remaining wall-normal gradient is then obscured by the boundary layer that develops between rows of turbines in the array.

The largest single component of the Reynolds stress tensor is the streamwise normal stress \overline{uu} , shown in Figure 4(b). Very near to the device at $x/D = 0.5$, the passage of the rotor is evident in the concentric circular arcs following the tip and root of the wind turbine blade. The mast is seen at $z/D = 0$ in the near wake but is washed out beyond $x/D \approx 2.5$. The normal stress \overline{uu} is most evident as a crescent-shaped structure following the outer portion of the wind turbine blades above $y/D \approx 0.75$. In the far wake, \overline{uu} is quite small and more homogeneously distributed throughout the measurement windows. The other diagonal components of the Reynolds stress tensor \overline{vv} and \overline{ww} (omitted from the current results for brevity) show spatial complexity only very near the wind turbine ($x/D \leq 1.5$).

Figures 4(c)–4(e) show the turbulence shear stresses for the wake. Peak magnitudes of $-\overline{uv}$ and $-\overline{uw}$ are approximately 1/3 the magnitude of \overline{uu} but show similar spatial development throughout the wake. Figure 4(c) shows $-\overline{uv}$ to have a complicated structure reflecting the rotation of the rotor and the geometry of the blades in the near wake. There, the region of negative shear is confined to the area immediately following the rotor below hub-height. As the flow mixes, $-\overline{uv}$ becomes more evenly distributed, the negative shear stress becomes nearly even throughout the lower half of the wake. Magnitudes of the Reynolds shear stress in the region where we observe the positive shear stresses are three times more intense than the region where the Reynolds shear stress is negative. The difference of extremes confirms that the entrainment of high-momentum flow into the wake is predominantly downward from above. Reflecting the findings of previous studies,^{12,13} the region in which $-\overline{uv} > 0$ drifts away from the wall in the far wake.

The streamwise-spanwise Reynolds shear stress is approximately antisymmetric about the xy -plane, shown in Figure 4(d). As discussed above, $-\overline{uw}$ shows the effects of rotation of the rotor blade in the near wake as a sinuous line distinguishing the positive and negative contributions to the field. Like \overline{uu} and $-\overline{uv}$, the peak value of $-\overline{uw}$ occurs at $x/D = 1.5$. Along the streamwise coordinate, the distinguishing line between positive and negative contributions is smoothed out although it maintains a slant toward the upper-left corner of each window. Current literature^{3,4,11} discusses the entrainment process as occurring primarily in the vertical direction. This is true when considering the canopy as a single entity, as the vertical direction is the only unconstrained direction. However, if modeling of the near wake including rotational effects and lateral entrainment is desired, $-\overline{uw}$ cannot be neglected in the entrainment process. Gradients of U with respect to wall-normal and spanwise directions are the same order of magnitude in the near wake, thus the lateral flux of kinetic energy $F_{1,3} = -\overline{uw}U$ is nearly equal to the vertical flux $F_{1,2} = -\overline{uv}U$. In the far wake, the spanwise gradient of the mean velocity is nearly null while the wall-normal gradient persists due to presence of the wall, resulting in

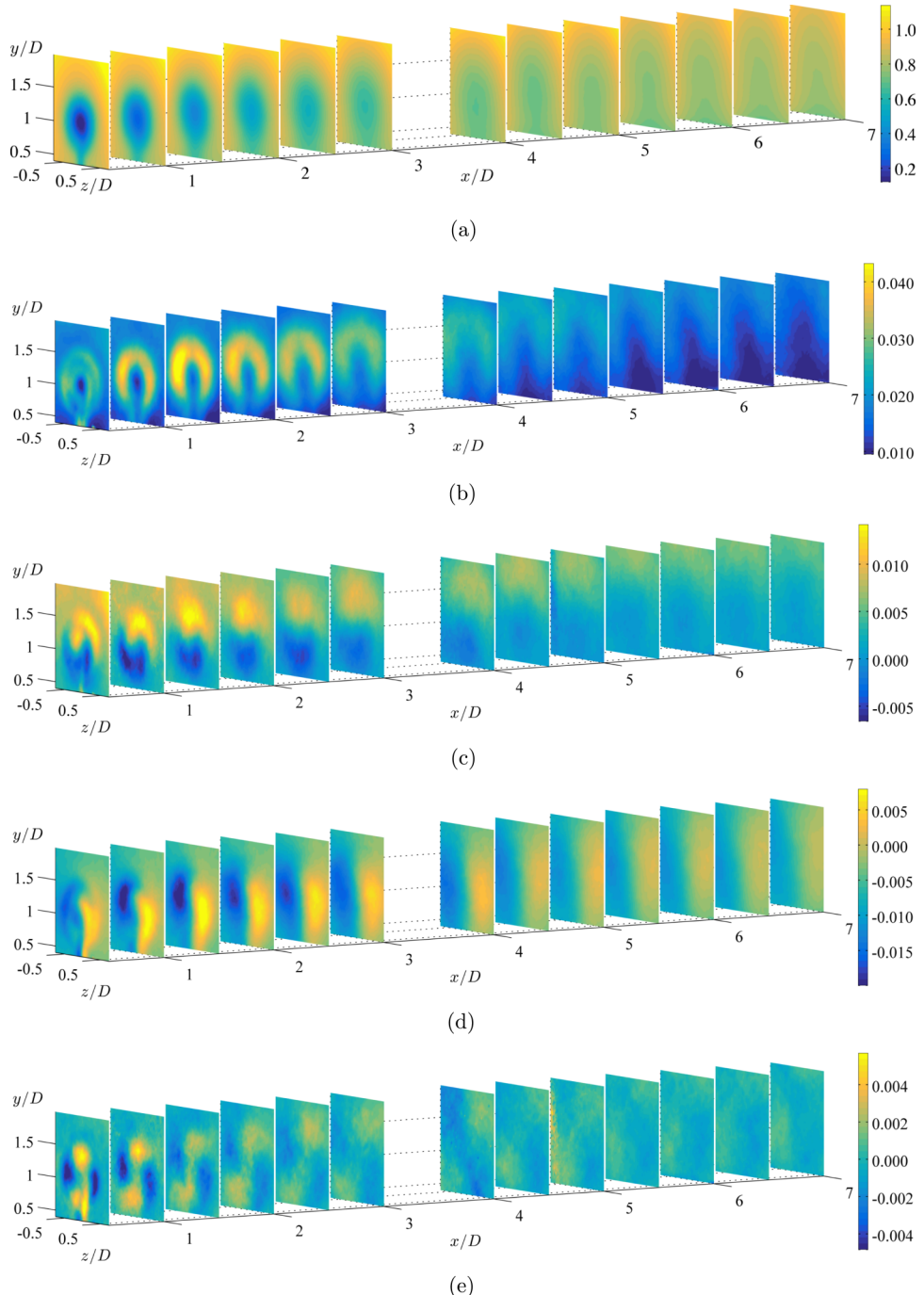


FIG. 4. Flow statistics for wind turbine wake. Flow is from left to right. (a) Normalized mean streamwise velocity U/U_{hub} , (b) normalized streamwise normal stress $\bar{u}\bar{u}/U_{\text{hub}}^2$, (c) normalized shear stress $-\bar{u}\bar{v}/U_{\text{hub}}^2$, (d) normalized shear stress $-\bar{u}\bar{w}/U_{\text{hub}}^2$, and (e) normalized shear stress $-\bar{v}\bar{w}/U_{\text{hub}}^2$.

flux vertically downward. Due to the softening of gradients ($\frac{\partial U}{\partial z}$ and $\frac{\partial U}{\partial y}$), production of turbulence kinetic energy is very small in the far wake.

The in-plane shear stress $-\bar{v}\bar{w}$ is shown in Figure 4(e). At its peak, $-\bar{v}\bar{w}$ is an order of magnitude smaller than the streamwise normal stress. Very near to the wind turbine model, there is evidence of the mast extending the positive region of $-\bar{v}\bar{w}$ to the bottom of the measurement window. The structures of $-\bar{v}\bar{w}$ diffuse outward from the nacelle of the turbine with x/D . The in-plane component

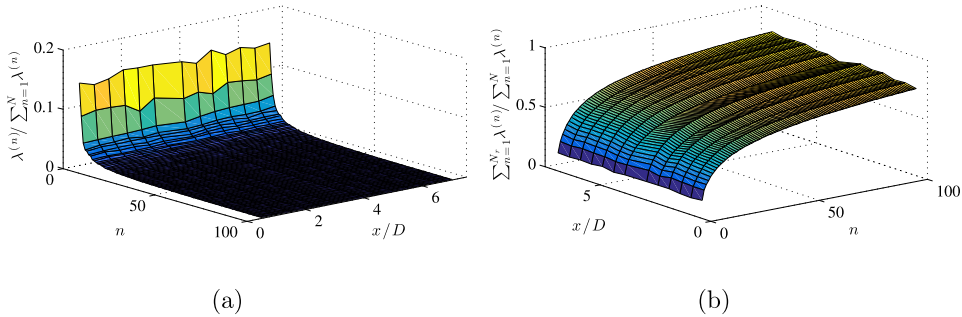


FIG. 5. Eigenvalues of the POD ($\lambda^{(n)}$) according to streamwise coordinate, (a). The normalized cumulative summation of eigenvalues is shown in (b). Only the first 100 eigenvalues are included.

demonstrates the lowest magnitude of the Reynolds stress tensor and the smallest signal-to-noise ratio in the current measurements. Because the mean spanwise velocity falls off quite quickly, the fluctuating spanwise velocity quickly becomes large relative to W and shows the slowest statistical convergence. Measurement error can be seen at $x/D = 4$, showing a slightly more intense negative region of $-\bar{v}\bar{w}$ than the other planes, and $x/D = 5$ where a reflection amplifies noise at $z/D \leq -0.5$.

A. POD results

The snapshot POD was applied to each measurement set separately, at each downstream location from $0.5 \leq x/D \leq 7$. Decomposition resulted in a total of 13 sets of POD modes $\Phi^{(n)}(x/D)$, each with 2000 modes. Additionally, eigenvalues $\lambda^{(n)}(x/D)$ for each set and the mode coefficients used in velocity field reconstruction $a_n(x/D)$ are produced in the proper orthogonal decomposition. If each POD mode is considered a degree of freedom (DOF) of the turbulent flow in the wind turbine wake, the total basis of the measured system is formed of 26 000 DOF, 13 locations \times 2000 modes each.

The complexity of the turbulent wake makes modeling the full range of dynamics and behavior prohibitively difficult, if not impossible. The eigenvalues associated with each mode delineate the relative importance and integrated turbulence kinetic energy expressed by velocity field projections onto each mode. Figure 5(a) shows the distribution of eigenvalues as a surface in x/D and mode number n . The cumulative fraction of $\lambda^{(n)}$ is shown in Figure 5(b) for the first 100 modes at each measurement location.

Common practice with the POD is to use the sequence of eigenvalues to determine at which point a truncation to the basis may be made, reducing the complexity of the flow description. It is quite common to set an arbitrary threshold of energy as the truncation point. Figure 6 shows the number of modes required to account for given thresholds of TKE throughout the wake. Note that very few modes (≈ 13) are required to reach the 50% of the energy in the measurement set, whereas many are required to restore 90% of the energy (≈ 350).

Figures 7 shows the first POD mode associated with streamwise, wall-normal and spanwise directions for each measurement location. In the near wake, evidence of the rotor is seen in every component of the modes and rotation can be seen throughout the wake as slight asymmetry about

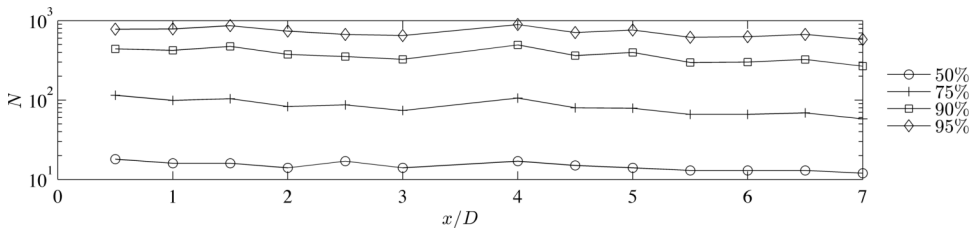


FIG. 6. Cumulative fraction of λ according to streamwise coordinate. The number of modes required to reach the listed thresholds are nearly constant in the wake.

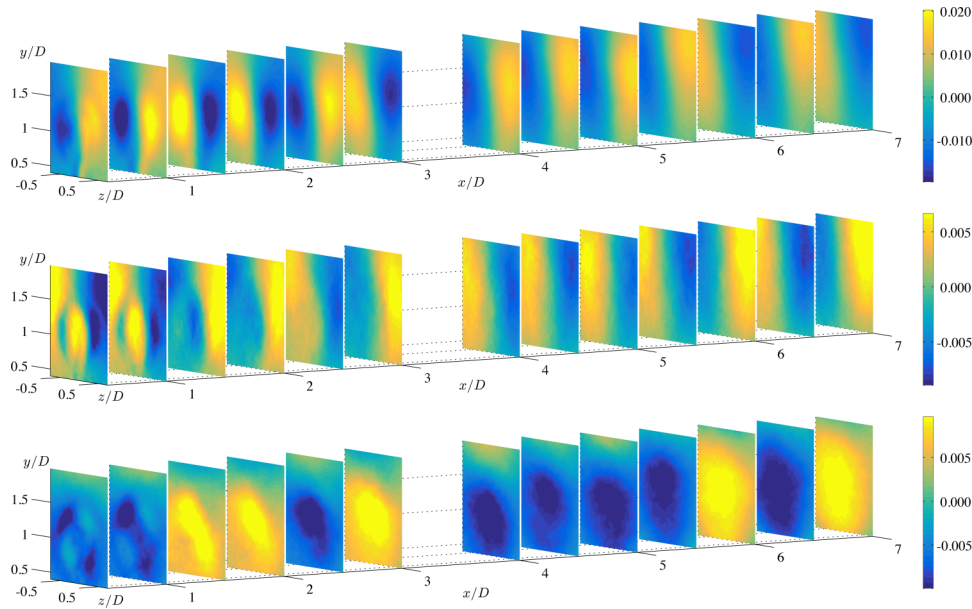


FIG. 7. POD mode 1 in the wake. From top are the ϕ_u , ϕ_v , and ϕ_w components.

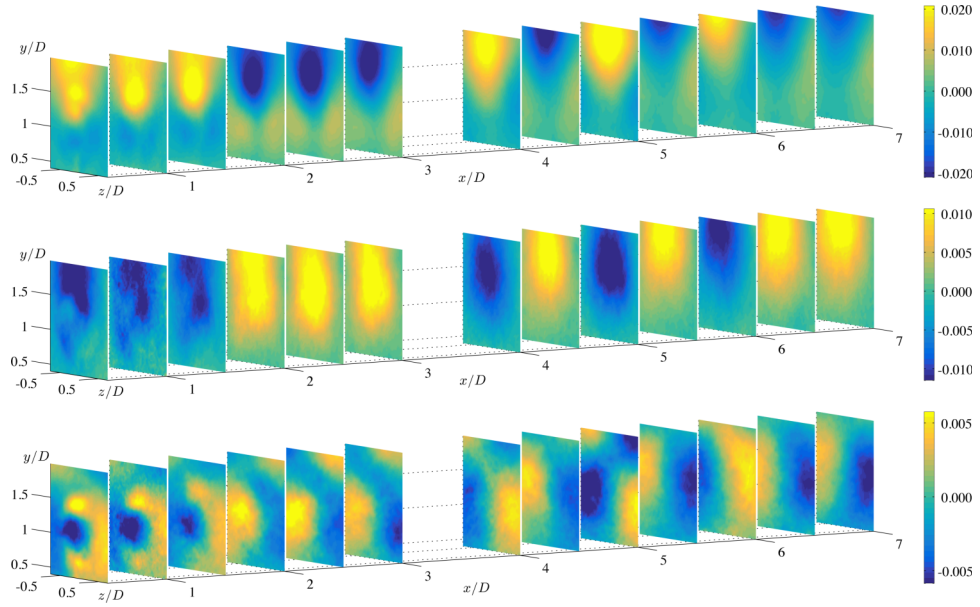
$z/D = 0$ into the far wake. Beyond $x/D \geq 2$, it is difficult to associate any particular structure in the modes to the passage of the rotor blades. The streamwise and wall-normal components of the first POD modes are roughly antisymmetric in the far wake. There, the spanwise component $\phi_w^{(1)}$ is nearly homogeneous in the measurement area with the exception of the shear layer present at the uppermost edge of the wake at $y/D \approx 1.75$. Antisymmetry seen in the stress $-\bar{uw}$, plotted in Figure 4(d), is visible in the streamwise component of the first POD mode $\phi_u^{(1)}$. The quadrant-like structure seen in $-\bar{vw}$ is seen in $\phi_w^{(1)}$.

Low modes are remarkably consistent throughout the wake along x/D . The streamwise component of the first POD mode $\phi_u^{(1)}$ is roughly antisymmetric about the center of the field at $z/D = 0$. However, the algebraic sign of the mode changes along x/D . The sign dependence of the modes is arbitrary in the basis, but corrected in the reconstruction with the respective coefficients $a_n(x/D)$. The coefficients can take either positive or negative values, and in linear combination with the modes lead to an algebraically consistent contribution to the Reynolds stress tensor.

The second POD mode shown in Figure 8 is independent of the first mode as the formulation of the POD requires that each mode maintains orthogonality with the others. The vertical component $\phi_v^{(2)}$ is expressed in a single peak with consistent magnitude and is centered in the spanwise direction following the wind turbine. As with $\Phi^{(1)}$, the second mode does demonstrate variation in the very near wake related to the passage of the rotors. The streamwise component $\phi_u^{(2)}$ exhibits a large structure above hub-height that contributes to the structure of $-\bar{uv}$. The relationships of the modes to the Reynolds stress tensor are otherwise not as clear as for $\Phi^{(1)}$.

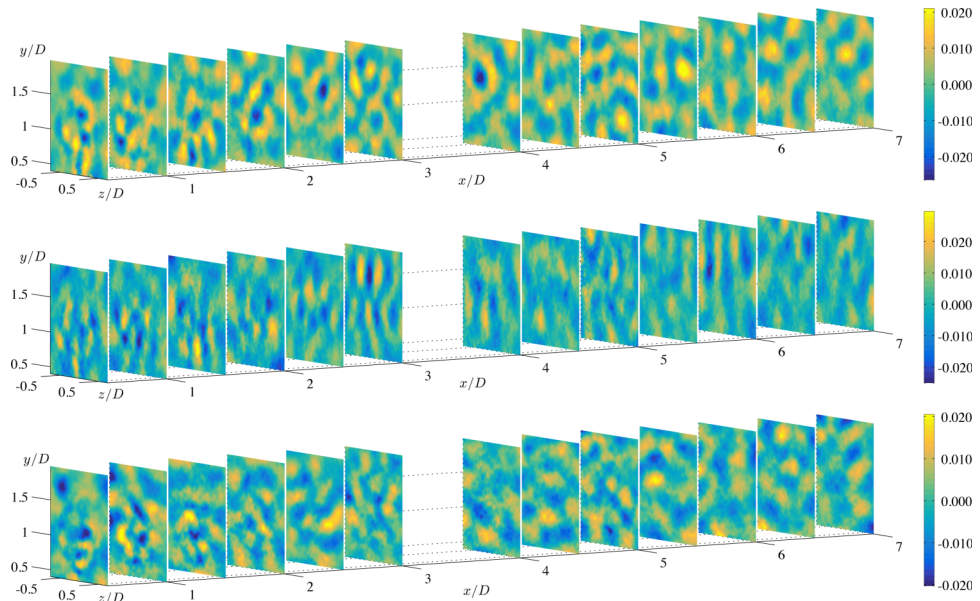
The flexibility of the algebraic sign shown in the first mode is also seen in $\Phi^{(2)}$. Interestingly, the locations that favor one sign over another are not consistent from mode to mode (e.g., at $x/D = 1.5$). Although generally considered to have the least significance and associated energy in the wake, the spanwise component $\phi_w^{(2)}$ shows more complexity than other components. At this mode number, there are still clear common projections in each snapshot basis. According to the cumulative summation of eigenvalues shown in Figure 5(b), $\Phi^{(1)}$ and $\Phi^{(2)}$ together account for approximately 25% of the integrated turbulence kinetic energy.

The intermediate range of POD modes is characterized by a loss of common projections. For modes above $n \approx 15$ it becomes very difficult to distinguish any coherent features. Figure 9 shows $\Phi^{(100)}$, chosen as a representative mode of intermediate rank. The eigenvalues provide a measure of the importance of each mode in the total flow. Normalized eigenvalues are consistent for all measurement

FIG. 8. POD mode 2 in the wake. From top are the ϕ_u , ϕ_v , and ϕ_w components.

locations and rapidly decrease in order of magnitude. The eigenvalues associated with the first mode ($\lambda^{(1)}(x/D) \approx 0.14$) and the hundredth mode ($\lambda^{(100)}(x/D) \approx 0.0003$) indicate the relative importance of each mode. As for $\Phi^{(100)}$, the modes of intermediate n do not exhibit structural consistency in the wake.

Truncating the POD basis and reconstructing the stresses according to Equation (9) yields Reynolds stresses filtered to include only the energetic turbulence structures. Figure 10 shows reconstructions of three stresses using a local threshold of 50% TKE (circle markers in Figure 6). The reconstruction of $\bar{uu}|_{50\%}$ in Figure 10(a) exhibits the crescent-shaped structure more clearly than the original statistics, since some of the small scale structures have been omitted. At $x/D = 0.5$, the

FIG. 9. The 100th POD mode, $\Phi^{(100)}$. Spatial organization into large structures is not evident in any but low mode numbers. From top are the ϕ_u , ϕ_v , and ϕ_w components.

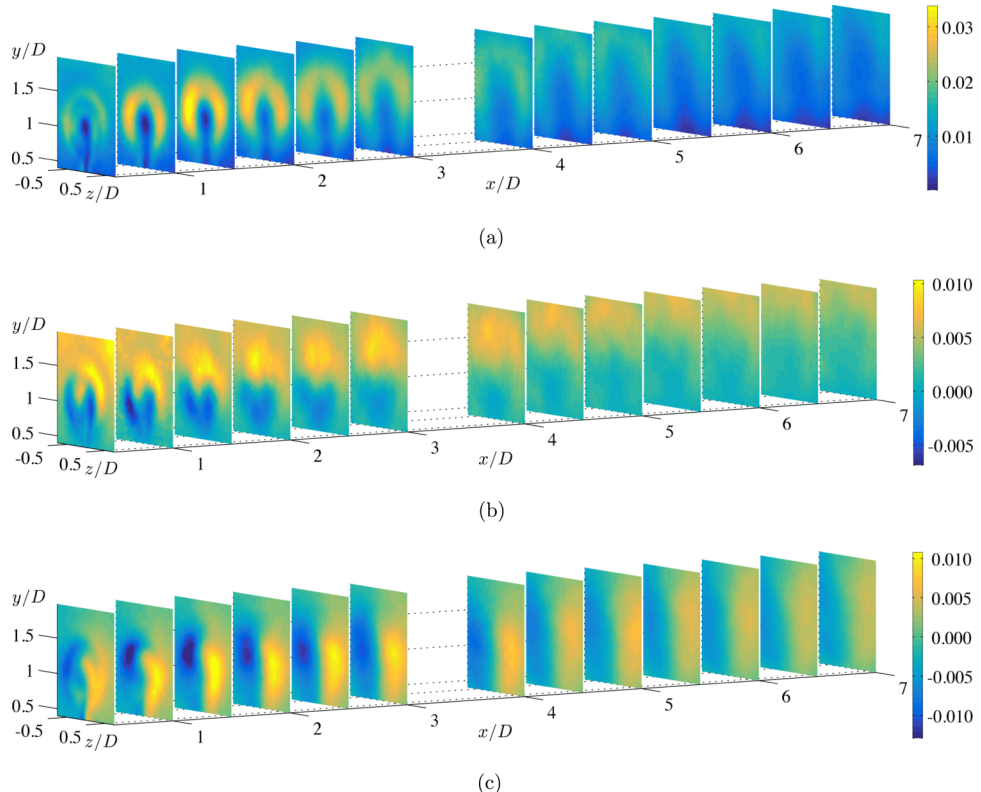


FIG. 10. Reconstructions of turbulence stresses based on 50% energy delineated by the cumulative fraction of λ . (a) $\hat{\bar{u}}\hat{u}|_{50\%}/U_{\text{hub}}^2$, (b) $-\hat{\bar{u}}\hat{v}|_{50\%}/U_{\text{hub}}^2$, and (c) $-\hat{\bar{u}}\hat{w}|_{50\%}/U_{\text{hub}}^2$.

reconstruction shows two lobes rather than the concentric rings in the original contour plot. In the far wake $x/D \geq 4$, the crescent is more angular than the unfiltered statistics, arising from the truncated basis used in the reconstruction. A maximum of 14 modes are required to reach the 50% thresholds used here according to the trend in Figure 6.

Shear stresses reconstruct much more ably than the normal stress as previously discussed. Figures 10(b) and 10(c) are quite similar in structure and magnitude to the original unfiltered statistics. The figure also shows that complex asymmetric structures arising from the passage of the rotors are represented well with a reduced POD basis. The shear stresses $-\hat{\bar{u}}\hat{v}|_{50\%}/U_{\text{hub}}^2$ and $-\hat{\bar{u}}\hat{w}|_{50\%}/U_{\text{hub}}^2$ are nearly identical to the conventional turbulence statistics at $x/D = 0.5$. This is also the location of the most structurally complex flow in the wake.

B. DPOD results

Modes shown above in Figures 7–9 were concatenated into bases of fixed mode number to form the snapshot bases for the DPOD. The procedure follows the work by Siegel *et al.*²⁵ with the exception that DPOD now offers decomposition over a spatial coordinate, further reducing the dependence of the resulting sub-modal basis to the in-plane spatial coordinates. The streamwise dependence is then accounted for by the series of, $b_{n,m}(x)$. Time dependence of the basis is already accounted for by the random coefficients of the original snapshot POD, $a_n(t)$. Application of the POD over concatenated sets of modes of common rank is shown as the step from point (C) to (D) in the conceptual diagram found in Figure 1.

Secondary application of the POD was the chosen method of assessing the evolution of modes in a streamwise direction due to its nature to filter important structures to front of the vector basis and less important structures to the end. Because the POD organizes structures in terms of common projection

and recombines through linear processes, it effectively ignores the switching of the algebraic signs seen above. Figures 7 and 8 demonstrate the organization and structural similarity of modes along the wind turbine wake. That the intermediate and high mode numbers do not show the same degree of organization throughout the wake is not surprising; less coherent turbulence structures that lack the energy necessary to persist throughout the wake.

Unlike the original application of the POD, the mean value of the kernel was *not* removed before decomposition. Therefore, the first mode in the resulting set of basis functions is the largest common projection between the POD modes and is representative of the mean of each mode,

$$\Gamma^{(n,1)} \approx \langle \Phi^{(n)} \rangle. \quad (15)$$

The plots of $\Phi^{(1)}$ and $\Phi^{(2)}$ (Figures 7 and 8) indicate that although the structure of the POD modes shows a consistent form throughout the wake, the algebraic signs of the modes often switch. During the reconstruction of fluctuating velocity fields, the coefficients a_n can take on negative values which accounts for the differences in mode signs from one measurement location to the next. However, the sign switching renders conventional statistics inadequate, as averaging a sign switching field may lead to misleading results.

As with the POD, the DPOD yields a set of orthogonal basis functions ($\Gamma^{(n,m)}$) and associated eigenvalues $\Lambda^{(n,m)}$ that communicate the relative importance of each basis function. It should be stated that in the first POD applied directly on the velocity field, the eigenvalues $\lambda^{(n)}$ relay the relative importance of $\Phi^{(n)}$ in terms of energy. Because the snapshot basis of the DPOD is made of unitless eigenmodes of the first decomposition, the eigenvalues resulting from the DPOD $\Lambda^{(n,m)}$ are unitless as well. The span of DPOD eigenvalues $\Lambda^{(n,m)}$ is shown in Figure 11. The figure illustrates that the weighted distribution expressed by the DPOD eigenvalues is a function of both the POD mode number n and sub-mode number m . For low mode numbers (n and m), the modes are organized in the wake and share structural elements. Organized modes have a few important substructures and $\Lambda^{(n,m)}$ falls off quickly. Increasing mode number yields structures that are less organized throughout the wake. At higher mode numbers, the distribution of $\Lambda^{(n,m)}$ is nearly homogeneous across the span of substructures. The flattening of the distribution implies that the sub-modal projections become more equal and that there are fewer identifiable trends in the POD mode in the wake.

To illustrate the significance of the sub-modes outlined in Figure 11, several DPOD bases are shown in the following figures. The decomposition of $\Phi^{(1)}$ into sub-modal structures, shown in Figure 12, illustrates the consistency of the modes in the wake. The distribution of $\Lambda^{(1,m)}$ shows that the importance of the sub-modal structures progressing in m varies over several orders of magnitude. The sub-modes are well organized for low sub-modal numbers but lose coherence and appear noisy for $m \geq 6$. Each plane is now a sub-modal component forming the basis of $\Phi^{(2)}$. The three components of the vectorial sub-modes are shown in the same format as the POD modes above for consistency, from top are the spans of $\gamma_u^{(1,m)}$, $\gamma_v^{(1,m)}$, and $\gamma_w^{(1,m)}$. The ordinate now represents the sub-mode number m rather than the streamwise coordinate. The first plane in each subfigure is the effective mean mode throughout the wake, immune to the switching of algebraic sign shown in the POD modes. Following the effective mean structure are corrections to the modal bases in order of significance of projection. The second and third sub-modes correspond well with features seen in the near wake of $\Phi^{(1)}$. Areas roughly sketching the swept area of the rotor are highlighted in sub-modes $m = 2, 3$, and 5 in γ_u and

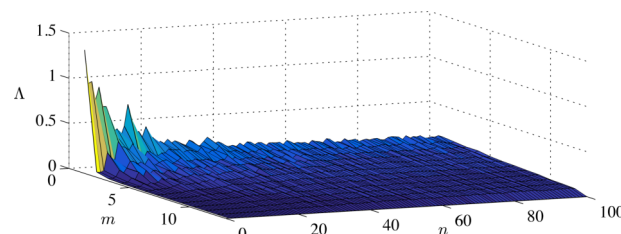


FIG. 11. Distribution of eigenvalues associated with each sub-modal structure in wind turbine wake.

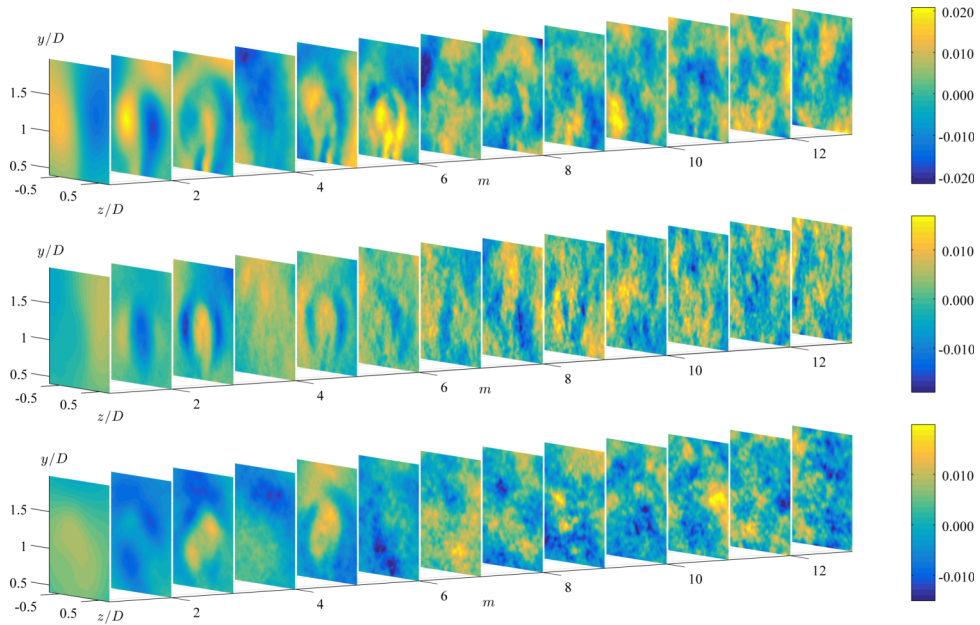


FIG. 12. Span of the first set of DPOD modes, $\Gamma^{(1,m)}$. From top are the γ_u , γ_v , and γ_w components.

γ_v , but are not as clear in γ_w . That the first sub-mode does not show effects from the rotor indicates that near-wake features are secondary to the underlying wake structure.

Similar levels of organization are seen in the span of $\Gamma^{(2,m)}$ in Figure 13. The sub-modes for $m \leq 4$ demonstrate coherent and organized features within the measurement fields but at higher sub-mode numbers, the coherence is lost and the fields appear noisier. As with $\Gamma^{(1,m)}$, sub-modes of $\Phi^{(2)}$ are thought of as a “starting” structure (effective mean, first sub-mode, $m = 1$) followed by progressively detailed adjustments. Several of the sub-modes exhibit Fourier-type behavior seen especially in the third sub-mode $\Gamma^{(2,3)}$. Applying the decomposition over homogeneous data results in a simplification of POD modes to Fourier modes.^{8,19,28} The second POD mode displays some homogeneity, especially related to the vertical component $\phi_v^{(2)}$, and some Fourier-like behavior in the sub-modal structures is expected. However, this type of behavior is not seen in all sub-modes.

Sub-modes of intermediate POD mode numbers such as $\Gamma^{(100,m)}$ demonstrate no discernible change in organization across the span of m , validating the hypothesis that only the first few POD modes carry energy through the wake. Comparing the POD mode from Figure 9 to the DPOD modes in Figure 14, one sees distinct differences from mode to mode, but not more organization. This indicates that there are no common projections of the POD modes characterized by intermediate and higher values of n and that not much new information is gained by application of DPOD.

Similarity of projections is also evident in the flattening of distributions of $\Lambda^{(n,m)}$ in Figure 11. When this is the case, the reconstruction coefficients associated with sub-modal structures $b_{n,m}$ do not show any preference for low sub-mode numbers and are more uniform across the span of m . The span of sub-mode coefficients is shown in Figure 15, decaying coefficients with m for low mode number n . At high mode number, $b_{n,m}$ shows no obvious dependence on m .

The coefficients are important in reconstructing the POD modes from a truncated set of sub-modal structures according to Equation (14). Each POD mode is represented as a linear combination of sub-modes with coefficients like those shown in Figure 15. The coefficients in the figure do not convey units as they do with the POD coefficients a_n . An important point regarding $b_{n,m}$ is that the coefficients are functions of the streamwise coordinate while the DPOD modes themselves are not. This implies that evolution of the original POD modes in the wake may also be described by the coefficients $b_{n,m}$.

The span of sub-modes $\Gamma^{(n,m)}$ can be truncated as for the POD. In doing so, the less organized sub-modal structures are omitted and linear combination then yields filtered POD modes $\Phi^{(n)}$. The sub-modes that are omitted are at least two orders of magnitude less significant than $\Gamma^{(1,1)}$. Because a

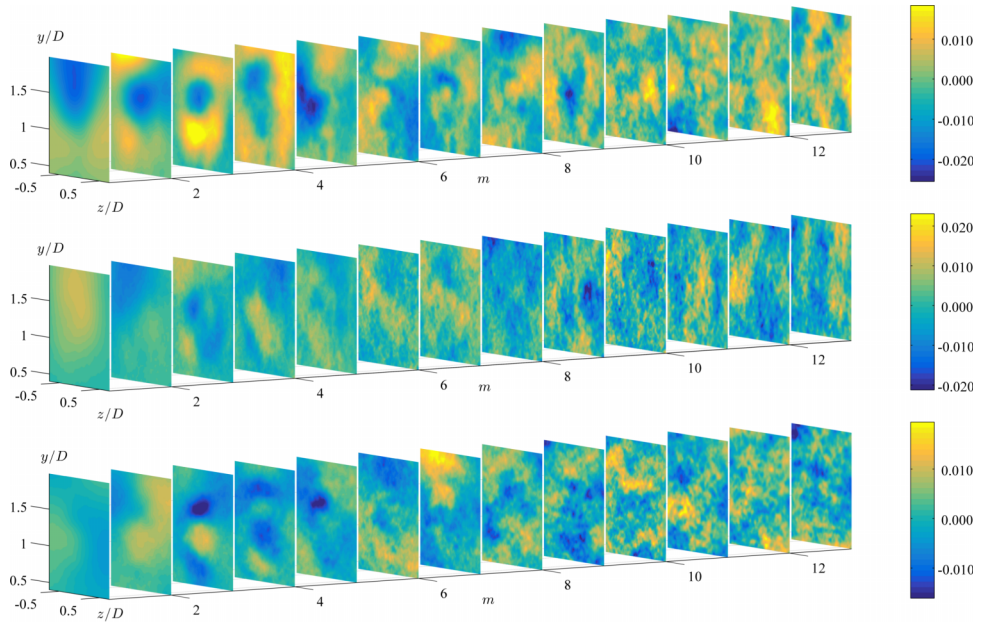


FIG. 13. Span of the second set of DPOD modes, $\Gamma^{(2,m)}$. From top are the γ_u , γ_v , and γ_w components.

series of filtered POD modes the desired outcome of the DPOD, each mode must be reconstructed with a truncated set of DPOD modes rather than using the method that reconstructs the kernel directly (Equations (13) and (14)). In this case, the D^n is not the desired output, but a series of low-order descriptions of the POD modes themselves. Mentioned earlier, the coefficients $b_{n,m}$ account for any sign switching seen in the POD modes.

Reconstructions of Reynolds stresses with POD modes at different degrees of filtering illustrate the contribution made by the first several sub-modes. Figure 16 compares the original shear stress $-\bar{uv}$ (left column) first to the low-order description with unfiltered POD modes. Filtering at the POD level $\bar{\bar{uv}}$ (second from left) is able to accurately rebuild the Reynolds stress tensor with only two modes.

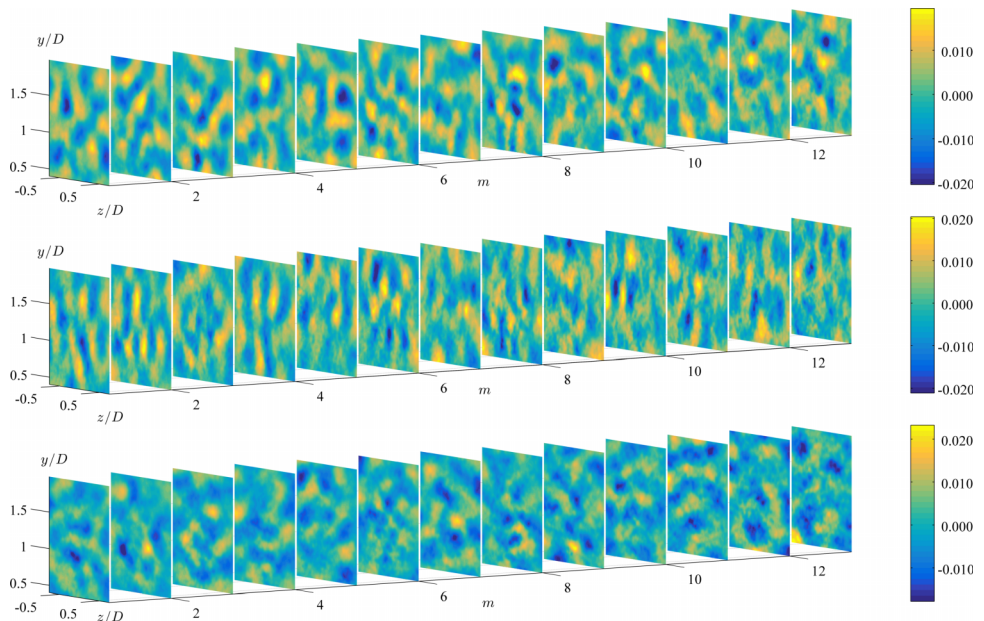


FIG. 14. DPOD of intermediate POD mode, $\Gamma^{(100,m)}$. From top are the γ_u , γ_v , and γ_w components.

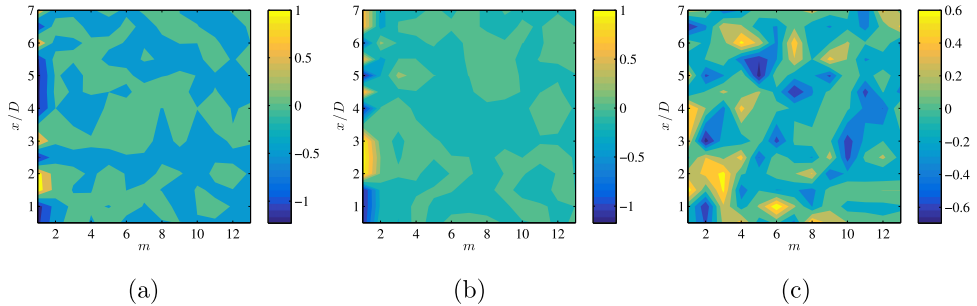


FIG. 15. Sub-modal coefficients $b_{n,m}$ associated with (a) $\Gamma^{(1,m)}$, (b) $\Gamma^{(2,m)}$, and (c) $\Gamma^{(100,m)}$.

However, despite similarity of either the original stress $-\bar{uv}$ or the stresses filtered at the POD level $-\bar{\dot{uv}}$, each downstream location must be reconstructed individually with independent sets of modes and eigenvalues. The double POD outlined above further reduces the necessary modes from $N_r \times 13$ degrees of freedom to a set of $N_r \times M_r$ sub-modes without considerable loss in accuracy.

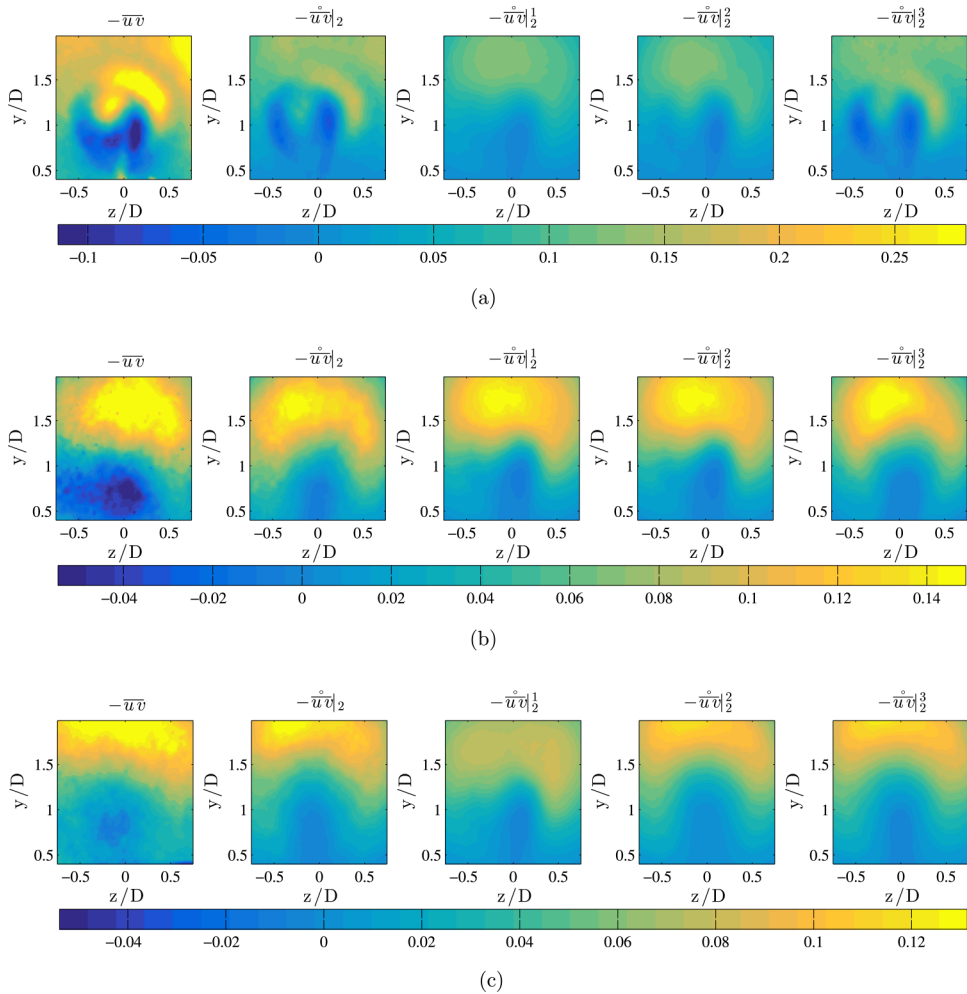


FIG. 16. Comparisons of the shear stress $-\bar{u}\bar{v}$ based on varying levels of sub-modal filtering. From left are the original statistical stress, the POD reduced order description, and the stress filtered with 1, 2, and 3 of the 13 sub-modes. (a) Reconstruction with sub-modal filtering at $x/D = 0.5$, (b) reconstruction with sub-modal filtering at $x/D = 3.5$, and (c) reconstruction with sub-modal filtering at $x/D = 6$.

Representations employing more sub-modes (relaxing sub-modal filters) in the description of statistics approach $-\dot{\bar{uv}}|_n$ with increasing span of m . The near-wake measurement locations show that the stress decreases in magnitude and effects of rotation decrease rather quickly. This is the range of the wake that exhibits the most complexity in the turbulence field. Looking to the third, fourth, and fifth columns of Figure 16, it is evident that the corrected stress reconstructed with sub-modal filtering ($-\dot{\bar{uv}}|_2^m$) is nearly identical from one location to the next. Increasing the number of sub-modes used to describe the basis functions leads to more distinct reconstructed stresses.

Structures of $-\dot{\bar{uv}}|_2^m$ appear to change with m , but quantitative comparison of $-\bar{uv}$ and the filtered descriptions in the following section indicates that they are quite similar. Evidence suggests that the accuracy of reconstructions does not change significantly beyond three modes either at the POD or the DPOD levels. This is taken as indication that the flow is dominated by only a few coherent turbulent structures that are well-characterized by the DPOD.

The following section details a direct method of correcting the range of dynamics in low-order descriptions of the Reynolds stress tensor with drastically reduced bases. The observation that the main features of the turbulence stresses in the wake may be reconstructed with very few modes suggests that the energy excluded must be fairly uniform or isotropic.

C. Corrected low-order description

In the context of the current work, the primary point of concern is finding a simplified means of describing the turbulent dynamics in wind turbine wakes. Increasing the number of POD modes used in the description increases the percentage of the turbulence kinetic energy represented. Successively more complex models (by the number of modes used) approach the original statistics used in the kernel.

POD applied to wind turbine wakes, discussed in Hamilton *et al.*,¹³ was shown to make a fair approximation of original statistics with as few as 1% of the total modes. In that work, the streamwise average of $-\bar{uv}$ and the associated components of the flux ($-\bar{uv}U$) and production ($-\bar{uv}\frac{\partial U}{\partial y}$) were analyzed in order to characterize the wake and approximations of it. A similar approach is undertaken below with specific profiles of the Reynolds stresses. Spatial averaging was determined to be inappropriate in the context of the current measurement set and aim of the model. Here, measurements are across the wakes and the in-plane spatial gradients are important considerations in the overall behavior of the wake.

Profiles of \bar{uu} and $-\bar{uv}$ are shown in Figure 17 are compared to profiles of the same stress modeled with bases reduced to varying degrees. In the figure, profiles in black represent quantities derived from the measured data. Gray profiles (light and dark) are statistics composed with a truncated basis of POD modes. As the number of modes increases, the POD representations approach the profile of the original statistics as expected. Using a single POD mode (profiles shown in dark gray solid lines) to represent the stress field in the wake is unable to capture the shape or character of the original statistics. The complex turbulence field in the wake cannot be reduced to a single eigenfunction. However, a description of the wake using two POD modes (profiles shown in dark gray dashed lines) is sufficient to reproduce the shape of the wake, if not the magnitudes of each stress. Profiles in light gray solid lines are those of composed with between 3 and 10 POD modes and demonstrate the tendency toward unfiltered statistics with larger modal bases.

This observation confirms that the lowest POD modes accounting for the large turbulence structures are responsible for the features of turbulence in the wake. Further, it confirms the hypothesis that reducing the modal basis is equivalent to excluding energy homogeneously from the wake. This suggests that a correction may be made to the low-order descriptions in the form of a simple constant to account for the turbulence kinetic energy in the excluded eigenvalues. The correction factor is a tensor of the form

$$\overline{u_i u_j} = C_{ij} \overline{\dot{u_i u_j}}|_n. \quad (16)$$

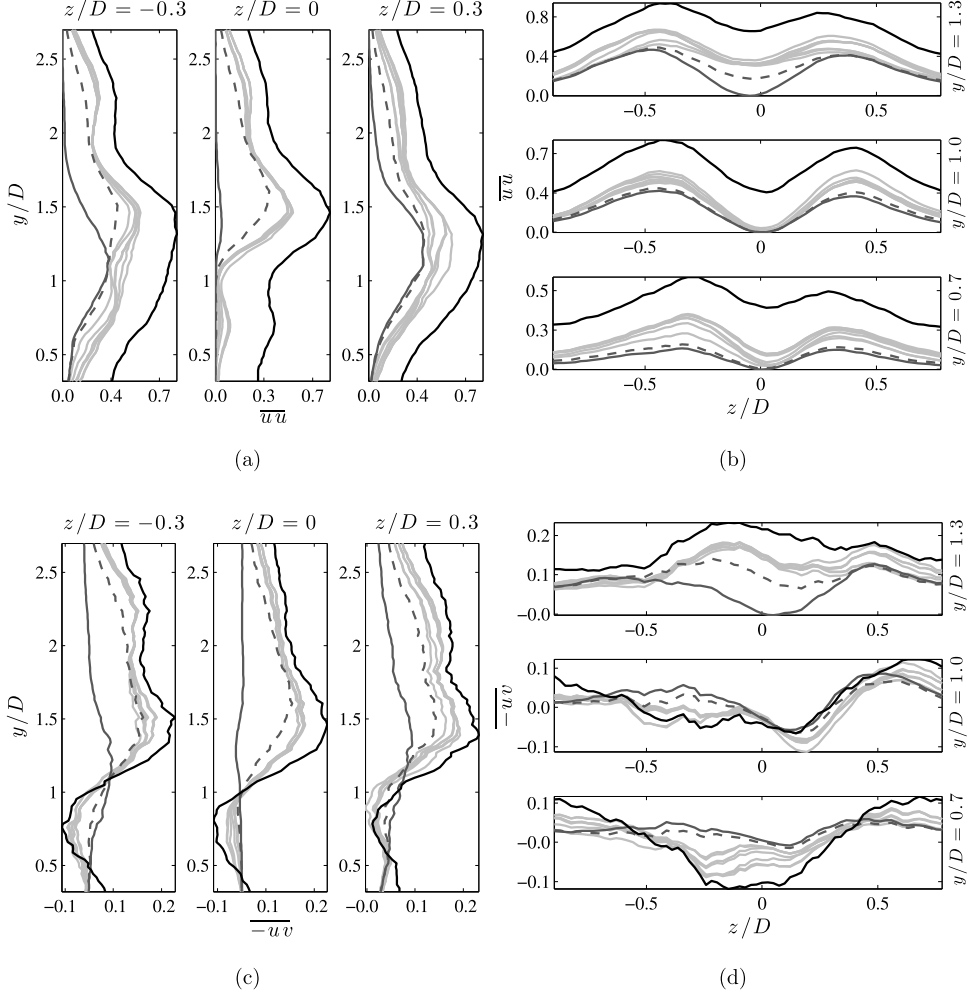


FIG. 17. Convergence of $\bar{\bar{u}}\bar{u}$ and $\bar{\bar{u}}\bar{v}$ to original statistical profiles using progressively more modes in reconstruction. Low-order descriptions with a single POD mode are shown as solid dark gray lines; descriptions with two POD modes dark gray dashed lines. Higher order descriptions are shown in light gray lines and the original statistics are shown in black. Profiles correspond to the data at $x/D = 1.5$, where the highest magnitudes of Reynolds stresses occur. (a) Vertical profiles comparing $\bar{\bar{u}}\bar{u}$ to $\bar{u}\bar{u}$, (b) Horizontal profiles comparing $\bar{\bar{u}}\bar{u}$ to $\bar{u}\bar{u}$, (c) Vertical profiles comparing $\bar{\bar{u}}\bar{v}$ to $\bar{u}\bar{v}$ and (d) Vertical profiles comparing $\bar{\bar{u}}\bar{v}$ to $\bar{u}\bar{v}$.

In Equation (16), the correction coefficient C_{ij} is found through a minimization of the root-mean-square (RMS) error, err_{ij} , between the statistical stress field and the corrected low-order description

$$C_{ij} \ni \min \left[\sqrt{\langle \bar{u}_i \bar{u}_j^2 - (C_{ij} * \bar{\bar{u}}_i \bar{u}_j|_n)^2 \rangle} \right] = \min [err_{ij}]. \quad (17)$$

The coefficient used to correct the range of statistics is a second-order tensor corresponding to the Reynolds stress tensor. The tensor C_{ij} accounts for the energy in the POD modes and λ values that are *not* used in the low-order description. Therefore, the expected behavior of the coefficient tensor is toward unity increasing the truncated basis used in the low-order description. The coefficient space for the corrected low-order description is shown in Figure 18 and confirms that C_{ij} approaches unity and that the RMS error tends toward zero as more POD modes are used in the low-order description; otherwise expressed as

$$\lim_{n \rightarrow N} C_{ij} = 1, \quad (18)$$

$$\lim_{n \rightarrow N} err_{ij} = 0. \quad (19)$$

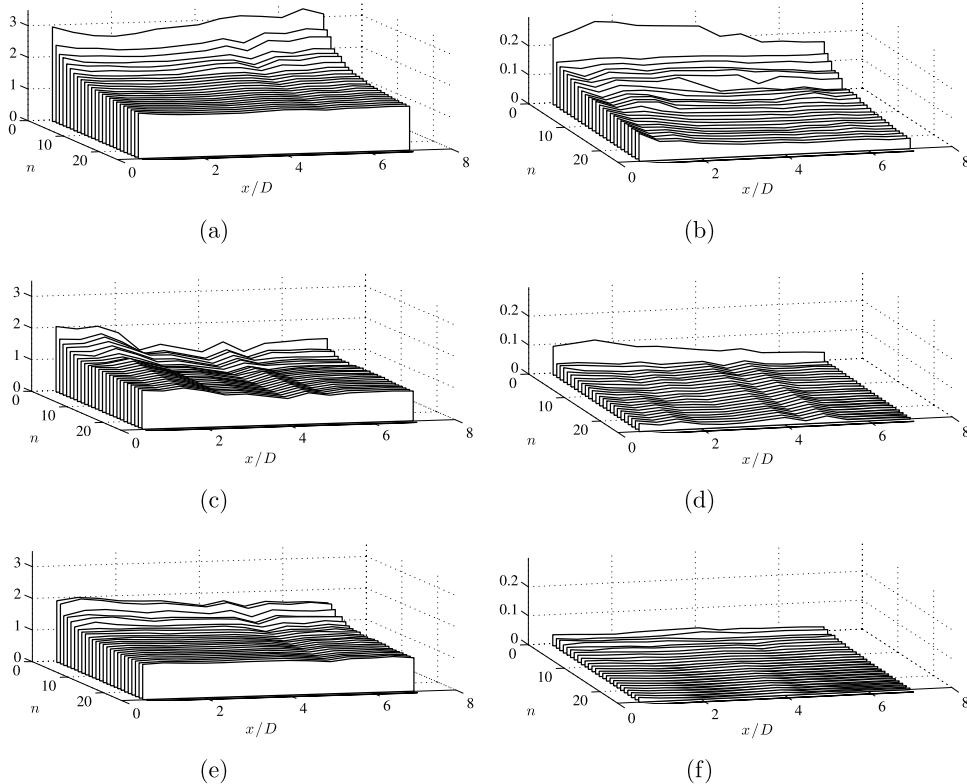


FIG. 18. Coefficients (left column) and error (right column) associated with correction of low-order descriptions of the streamwise normal stress ($\bar{u}\bar{u}$) and shear stresses responsible for entrainment ($-\bar{u}\bar{v}$ and $-\bar{u}\bar{w}$) as a function of number of modes used in low-order representation of stresses (n) and streamwise coordinate (x/D). (a) C_{11} , (b) err_{11} , (c) C_{12} , (d) err_{12} , (e) C_{13} , and (f) err_{13} .

Figure 18 compares the necessary correction and associated error for components of the Reynolds stress tensor involving fluctuations in the streamwise velocity, $\bar{u}\bar{u}_j$. The coefficient space indicates that both the correction and the RMS error is less for shear terms than for normal stresses. Including successively more POD modes aids in the reconstruction of the Reynolds stress tensor unevenly; it takes many modes to rebuild the diagonal components of $\bar{u}_i\bar{u}_j$ (normal stresses), whereas the character of shear terms is evident quite quickly, and the coefficient is near unity. The balance of the coefficients is necessarily dependent on the nature of the flow and may be further explored through an analysis of the turbulence anisotropy akin to that presented in Hamilton and Cal.¹⁰

Development of C_{ij} and err_{ij} associated with limiting the coefficient space to two POD modes is shown in Figure 19. The basis is limited according to the above observation that a minimum of two modes is necessary to reproduce the form of the stress field in the wake. Figure 19(a) shows that the correction needed for many of the stresses is nearly constant throughout the wake. This is taken as confirmation that the POD modes in the wake are related to one another and their evolution is described by additional simplifications. The exceptions to this observation are coefficients associated with the vertical and spanwise normal stresses. In these cases, C_{22} and C_{33} are more variable in the wake and are in the range of $4 \leq C_{ij} \leq 6$.

While C_{ij} is nearly constant for each stress, the error associated with the correction (Figure 19(b)) decreases slightly as the wake develops in the streamwise direction. Also clear in the figure is the distinction between accuracy of the low-order description of shear and normal stresses. In the near wake, the error in describing the diagonal terms of $\bar{u}_i\bar{u}_j$ is greater than 15%, difficult to consider a good approximation for any model. Recalling that only 0.1% (two modes) of the POD basis is being used, the RMS error is surprisingly low. More impressive is that the reconstruction of shear terms is accurate with error less than 5% even at $x/D = 0.5$, where the stress field is structurally complex.

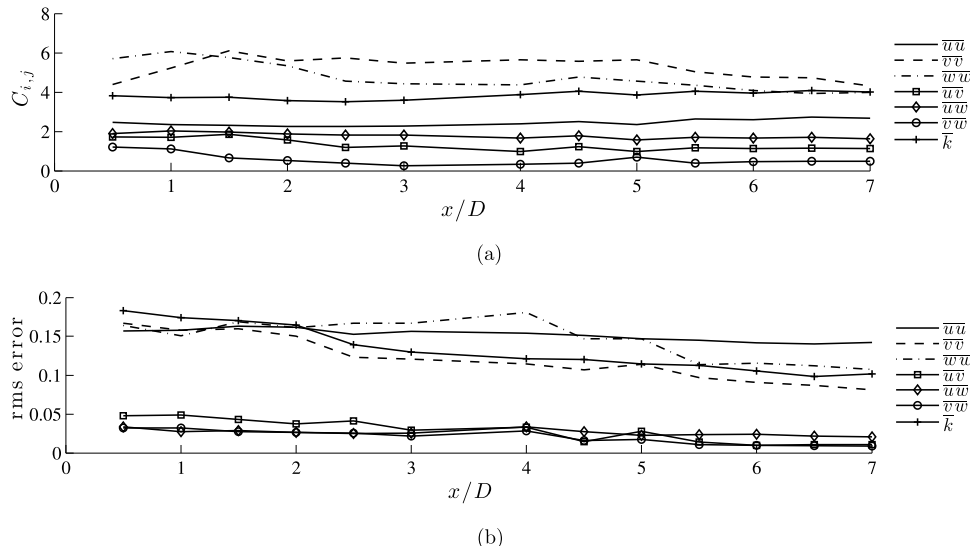


FIG. 19. Correction coefficient and associate error for severe reduction (two modes, $N_r = 2$). (a) Correction coefficient C_{ij} for each component in the Reynolds stress tensor and TKE versus streamwise coordinate x/D and (b) Root-mean-square error associated with the corrected description of stresses versus streamwise coordinate x/D .

The error of the low-order descriptions decreases in a roughly linear manner to approximately 3% for the shear stresses and in the range of 9%–14% for the normal stresses. Shown in Figure 17(a), the low-order representations of the normal stress $\bar{u}\bar{u}$ are unable to capture the location of peak values along the wall-normal coordinate. At the bottom of the measurement window, the reconstructions are nearly null. A simple correction coefficient is unable to account for this behavior through direct multiplication, and as a result the corrected low-order description underestimates the value of the stresses there.

Representations here do not make use of the DPOD outlined above; each plane requires a separate set of POD modes and eigenvalues to reconstruct the stress field using a total of 26 DOF. The comparisons in Figure 16 indicate that the stress field can again be simplified by filtering each of the POD bases. To determine at what level the sub-modal filtering should be applied, a coefficient space analogous to that of C_{ij} was mapped and analyzed. Minimizing correction error for the span of sub-modes increases the dimension of the coefficient space by one to include POD mode number n , downstream location x/D , and sub-mode number m .

Model correction with sub-modal filtering undertaken here limits the POD basis to only two modes. The coefficient space using sub-modal filtering is not shown here for the sake of space. However, using the full range of sub-modes $m = 13$, the coefficients match those of above (Figure 18) exactly. This conforms to expected results as using the full span of sub-modes is exactly equivalent no filtering at all, but requires additional steps in calculation.

Sub-modal filtering applied to the present measurement set showed that the total DOF of the wake could be further reduced without substantial sacrifice of accuracy of the description. Discussed above, the first sub-mode is an effective average of each POD mode in the wake, disregarding the alternation of the algebraic sign in Figures 7 and 8. Accordingly, the eigenvalue associated with the first mode is much larger than for the others. This relationship holds true for the reconstruction coefficients $b_{n,m}$ as well. These relationships imply that for small n , $\Phi^{(n)}$ may be accurately represented in the entire wake with only a truncated set of corresponding $\Gamma^{(n,m)}$. Filtering with two sub-modes increased the error associated with the corrected reduced-order model by approximately 6%.

As above, the coefficient and associated reconstruction errors may be considered approximately constant through the wake. The total simplification of the wake is now from 26 000 DOF to 4 DOF (two POD modes filtered to two sub-modes) and a constant. The wake has been simplified to approximately 0.015% of the original complexity through iterative application of the proper orthogonal decomposition. The corrected low-order description represents the normal stresses with accuracy on

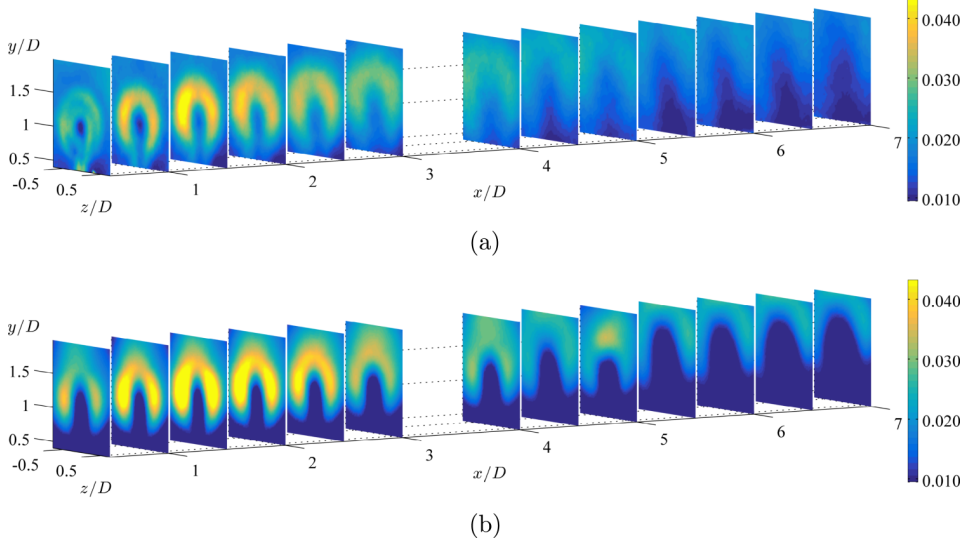


FIG. 20. Comparison of $\bar{u}\bar{u}$ to $C_{11}\bar{u}\bar{u}|_2^2$. The modeled normal stress diverges from the statistics most following the mast of the model wind turbine at $z/D = 0$. (a) $\bar{u}\bar{u}/U_{\text{hub}}^2$ and (b) $C_{11}\bar{u}\bar{u}|_2^2/U_{\text{hub}}^2$.

the order of 12%-15% and shear stresses to within 3%. The coefficient tensor and associated error, respectively, are now

$$C_{ij} = \begin{bmatrix} 2.45 & 1.31 & 1.78 \\ & 5.25 & 0.56 \\ & & 4.75 \end{bmatrix}, \quad \text{rms}_{ij}(\%) = \begin{bmatrix} 15 & 2.8 & 2.6 \\ & 12 & 2.0 \\ & & 15 \end{bmatrix}. \quad (20)$$

Figure 20 offers a comparison between the original streamwise normal stress derived through Reynolds averaging and that arising from the correction of the low-order description of the wake. For the streamwise normal stress in Figure 20(b), the obvious difference (and primary source of the error shown in Equation (20)) is an underestimation in the lower half of the measurement planes for $y/D \leq 1$. Low values of stress in the reconstruction are related to $\Phi^{(2)}$ having nearly null values below

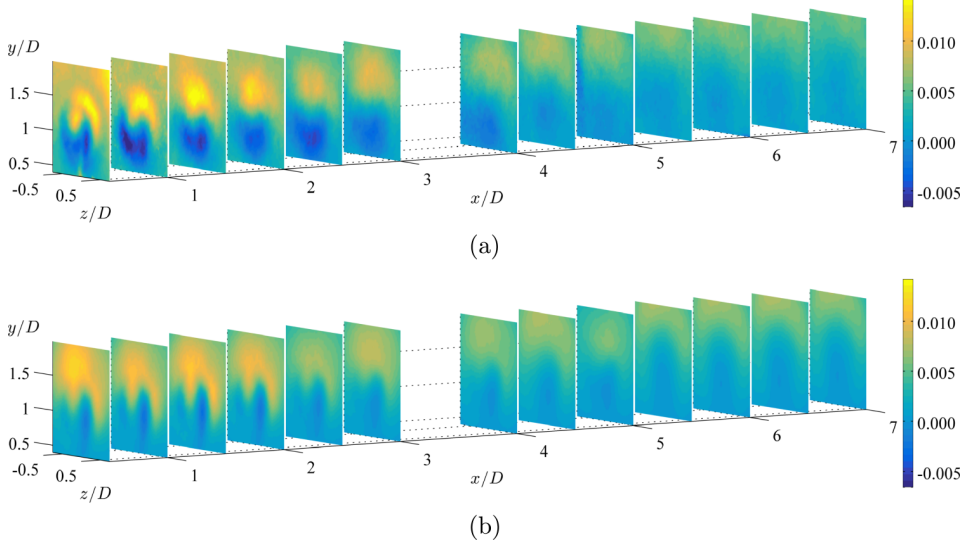


FIG. 21. Comparison of $-\bar{u}\bar{v}$ to $-C_{12}\bar{u}\bar{v}|_2^2$. Error associated with model correction is largely due to the overestimation of $-\bar{u}\bar{v}$ in the near wake at $x/D \leq 2$. (a) $-\bar{u}\bar{v}/U_{\text{hub}}^2$ and (b) $-C_{12}\bar{u}\bar{v}|_2^2/U_{\text{hub}}^2$.

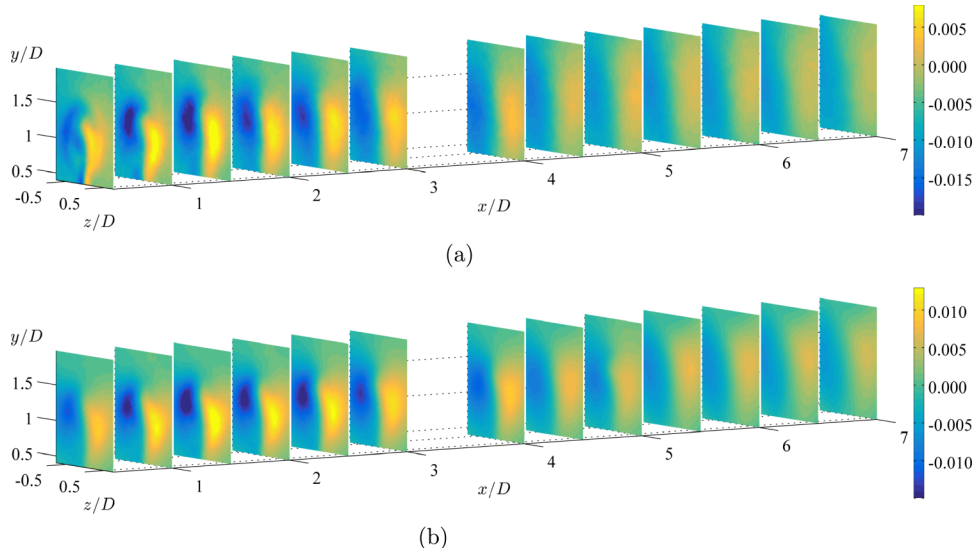


FIG. 22. Comparison of $-\bar{uw}$ to $-C_{12}\bar{uv}|_2^2$. Features in the near wake ($x/D = 0.5$) are simplified in the low-order description. (a) $-\bar{uw}/U_{hub}^2$ and (b) $-C_{13}\bar{uv}|_2^2/U_{hub}^2$.

hub-height. Through linear combination, local zeros in POD modes cannot contribute to stresses in the reconstructions. However, trailing the swept area of the blades above hub-height is the region of activity of \bar{uw} and is shown quite clearly in $\bar{uw}|_2^2$.

Shear stresses reconstruct with approximately 13% lower RMS error than the diagonal terms of $\bar{u}_i \bar{u}_j$. Figure 21 compares $-\bar{uv}$ and $-\bar{uv}|_2^2$. This is the component of the Reynolds stress tensor contributing most to the entrainment that drives the recovery of the wake, allows for energy extraction, and resupplies momentum for the wind farm as a whole. The reconstruction $-C_{12}\bar{uv}|_2^2$ represents the expected behavior in the wake to within 2.8%. It is somewhat surprising that a model reduction of this severity is able to reproduce the structures of turbulence in the full wake. The stress field evolves quickly in the near wake and demonstrates complex contours very near the turbine blades. The low-order representation underestimates regions of negative stress trailing the lower half of the turbine rotor. The model also exaggerates the structural complexity of the stress field in the same region. In the far wake ($x/D \geq 4$), the model appears to impart the wake with greater lateral symmetry than observed in the original statistics. Effects of this nature arise from the symmetry seen in the $\Gamma^{(n,m)}$.

The streamwise-spanwise Reynolds stress $-\bar{uw}$ is reproduced to within 2.6% in the corrected low-order description. Figure 22 confirms the accuracy of the model for $-\bar{uw}$. The error of 2.6% is largely associated with features directly following the rotor at $x/D = 0.5$. As with $-\bar{uv}$, the complexity of the stress field is estimated surprisingly well in the near wake. Fine-scale features are seen quite clearly trailing the top of the swept area of the rotor. In the far wake, the reproduction is accurate, showing discrepancies only above the turbine rotor $y/D \geq 1.5$, corresponding with the shear layer that develops between the wake and the flow above the turbine canopy.

V. CONCLUSIONS

The experiment undertaken accessed the flow via stereo particle image velocimetry resulting in instantaneous velocity measurements with spatial resolution of 1.4 mm between vectors in 13 planes parallel to the swept area of the rotors. Measurements acquired here illustrate the full Reynolds stress tensor and are able to highlight the shear stresses that contribute to the remediation of the wakes. Flow statistics near the wind turbine illustrate the spatially complex distribution of stresses in the wake and the progressively less intense gradients downstream of the turbine.

Applying the snapshot POD to the span of the two-points correlation tensor yields the optimal set of 2000 orthonormal eigenfunctions and eigenvalues that communicate the turbulence kinetic energy. Because the wake of a wind turbine is dominantly defined by the largest and most energetic turbulence structures, the POD is well suited to describing it via truncated bases and low-order descriptions. Decomposition of datasets recorded at different times and locations illuminated POD modes that were clearly related throughout the wake.

A multi-dimensional application of the proper orthogonal decomposition is developed for the complex flow in the wind turbine canopy. The current approach applies the snapshot POD in time, followed by decomposition about a spatial dimension. Resulting from the double POD is a set of sub-modal structures that span the mathematical space defined by POD mode of common rank throughout the wake. The DPOD as it is formulated here is able to assess the organization of the modes in the wind turbine wake as functions of the streamwise coordinate. Reconstructing the POD bases for each location in the wake is accomplished by linear combination of sub-modes with the set of coefficients that communicate their respective significance. Application of the POD through the wake transfers dependence on the streamwise coordinate of the wake sub-structures to a set of ordered coefficients. Use of the DPOD to characterize the spatial evolution of energetic POD modes is extended to other spatially developing flows with little modification.

Rebuilding the Reynolds stress tensor with truncated sets of POD modes necessarily excludes a portion of the turbulence kinetic energy accounted for in the original measurements. It is observed that while a truncated basis consisting of a single mode lacks the complexity necessary to describe the dynamics in the wake, a basis of two modes is able to capture the form, if not the magnitude of the stress field. Based on this observation, a tensor of coefficients is composed to account for excluded energy. The constants are optimized to minimize the root-mean-square error between the original statistics and the low-order description.

Coefficients used to correct the low-order description of turbulence in the wind turbine wake are taken as constants. While the coefficients are maintained as constant, the RMS error in the wake appears to decay linearly with downstream distance from the turbine rotor. Analogously, optimizing coefficients to correct the low-order description composed with POD modes filtered at the sub-modal scale further reduced the number of modes required to describe the wake with only a minor loss of accuracy. In this method, the wake is represented with approximately 0.015% of total degrees of freedom of the original measurement set while maintaining error of 15% for the normal components of the Reynolds stress tensor and less than 3% for the shear terms. Considering that the coefficient tensor accounts for energy excluded from the truncated basis, it is hypothesized that a detailed analysis of the turbulence isotropy may provide insight into the relative magnitude of each correction. The normalized Reynolds stress anisotropy tensor details the balance of energy in the turbulence stress field, providing a physical reasoning for the balance of terms in the correction tensor.

The above analysis demonstrates a method that is applicable to related sets of POD modes derived from SPIV measurements at multiple locations. The correction applied demonstrates that the energy excluded from the low-order description is nearly uniform background energy that influences the magnitude of turbulent stresses but contributes little in the way of discernible features. Influence of the rotor blades is illustrated by the DPOD, which separates the basis of POD modes into an average modal structure and distinct near- and far-wake contributions. That the shear terms in the wake accurately reconstruct with only small corrections suggests that they rely on high-energy, anisotropic turbulence preferentially represented by the POD. Modes that are not coherent in the wake are characterized by a nearly uniform distribution of sub-modal energy. Large-scale structures identified in previous applications of the POD to wind turbine arrays are out of reach in the current measurements, although the streamwise development of roller modes identified by VerHulst and Meneveau²⁹ would be well-characterized by the DPOD proposed here yielding insight into the entry length of the wind turbine array or the fully developed array condition.

Stress fields composed with the corrected low-order description show surprising complexity in the near wake and evolution of the turbulence field in the wake. Expanding the basis used in the reduced order description allows more subtle features to be expressed in the wake at the cost of overall model reduction. POD modes have been successfully used as the basis functions for predictions derived from the Galerkin method (see e.g., Kunisch and Volkwein,¹⁶ Lehmann *et al.*¹⁷). To that end,

POD modes are an ideal choice as they are derived from the flow in question and are the optimal basis for representing energy of the flow. Sub-modes derived through the DPOD may be combined with Galerkin projection in the same way, yielding further reduction in the number of basis functions needed. DPOD with correction modeling can simplify the Galerkin approach as the sub-modes exhibit the most characteristic features across the set of POD modes, which should increase model convergence. Alternative reduced order models employing POD modes include the use of artificial neural networks, as employed by Siegel *et al.*²⁵ There, neural networks were used as the basis for robust, numerically stable feedback flow control models. The current results are efficiently able to account for the turbulence shear stresses that contribute to bulk flow kinetic energy entrainment into the wake. With a basis of four sub-modal structures, the POD modes may be rebuilt for any point in the wake provided sub-modal coefficients are available.

In addition to a full order of magnitude further model reduction, the DPOD offers insight beyond the snapshot POD in several ways. The most significant is that the DPOD offers a means of characterizing the spatial development or evolution of POD modes. As the POD modes are agnostic to algebraic sign, traditional statistical approaches are difficult to apply. Additionally, the coefficients $b_{n,m}$ related to the DPOD modes are spatially explicit functions describing the influence of each sub-modal structure over the span of the DPOD domain. The DPOD not only relates and unifies measurement sets but also filters noise and errors arising from the initial eigenvalue decompositions, leading to cleaner functions to be used in the formation of reduced order models. As an extension of the proper orthogonal decomposition, the DPOD provides a means for further modeling approaches, in particular, the modeling of correction terms, which merits further investigation.

ACKNOWLEDGMENTS

The authors would like to acknowledge the U.S. National Science Foundation for supporting the above work. This material is based upon work supported by National Science Foundation IGERT Grant No. 0966376: Sustaining Ecosystem Services to Support Rapidly Urbanizing Areas. Any opinions, findings, and conclusions or recommendations expressed in this material are those of the authors and do not necessarily reflect the views of the National Science Foundation. Additional support from the Nation Science Foundation Grant Nos. NSF-ECCS-1032647 and NSF-CBET-1034581.

- ¹ N. Aubry, R. Guyonnet, and R. Lima, "Spatiotemporal analysis of complex signals: Theory and applications," *J. Stat. Phys.* **64**(3-4), 683–739 (1991).
- ² D. Bastine, B. Witha, M. Wächter, and J. Peinke, "Towards a simplified dynamic wake model using POD analysis," *Energies* **8**(2), 895–920 (2015).
- ³ R. B. Cal, J. Lebrón, L. Castillo, H. S. Kang, and C. Meneveau, "Experimental study of the horizontally averaged flow structure in a model wind-turbine array boundary layer," *J. Renewable Sustainable Energy* **2**, 013106 (2010).
- ⁴ M. Calaf, C. Meneveau, and J. Meyers, "Large eddy simulation study of fully developed wind-turbine array boundary layers," *Phys. Fluids* **22**, 015110 (2010).
- ⁵ L. P. Chamorro and F. Porté-Agel, "Turbulent flow inside and above a wind farm: A wind-tunnel study," *Energies* **4**(11), 1916–1936 (2011).
- ⁶ L. P. Chamorro, R. Arndt, and F. Sotiropoulos, "Turbulent flow properties around a staggered wind farm," *Boundary-Layer Meteorol.* **141**(3), 349–367 (2011).
- ⁷ L. P. Chamorro, R. Arndt, and F. Sotiropoulos, "Reynolds number dependence of turbulence statistics in the wake of wind turbines," *Wind Energy* **15**(5), 733–742 (2012).
- ⁸ J. H. Citriniti and W. K. George, "Reconstruction of the global velocity field in the axisymmetric mixing layer utilizing the proper orthogonal decomposition," *J. Fluid Mech.* **418**, 137–166 (2000).
- ⁹ W. R. Graham, J. Peraire, and K. Y. Tang, "Optimal control of vortex shedding using low-order models. Part I. Open-loop model development," *Int. J. Numer. Methods Eng.* **44**(7), 945–972 (1999).
- ¹⁰ N. Hamilton and R. B. Cal, "Anisotropy of the Reynolds stress tensor in the wakes of wind turbine arrays in Cartesian arrangements with counter-rotating rotors," *Phys. Fluids* **27**(1), 015102 (2015).
- ¹¹ N. Hamilton, H.-S. Kang, C. Meneveau, and R. B. Cal, "Statistical analysis of kinetic energy entrainment in a model wind turbine array boundary layer," *J. Renewable Sustainable Energy* **4**(6), 063105 (2012).
- ¹² N. Hamilton, M. Melius, and R. B. Cal, "Wind turbine boundary layer arrays for cartesian and staggered configurations. Part I. Flow field and power measurements," *Wind Energy* **18**(2), 277–295 (2015).
- ¹³ N. Hamilton, M. Tutkun, and R. B. Cal, "Wind turbine boundary layer arrays for cartesian and staggered configurations. Part II. Low-dimensional representations via the proper orthogonal decomposition," *Wind Energy* **18**(2), 297–315 (2015).
- ¹⁴ K. Hasselmann, "Pips and pops: The reduction of complex dynamical systems using principal interaction and oscillation patterns," *J. Geophys. Res.: Atmos.* **93**(D9), 11015–11021, doi:10.1029/JD093iD09p11015 (1988).
- ¹⁵ J. Kostas, J. Soria, and M. S. Chong, "A comparison between snapshot POD analysis of PIV velocity and vorticity data," *Exp. Fluids* **38**(2), 146–160 (2005).

- ¹⁶ K. Kunisch and S. Volkwein, "Galerkin proper orthogonal decomposition methods for a general equation in fluid dynamics," *SIAM J. Num. Anal.* **40**(2), 492–515 (2002).
- ¹⁷ O. Lehmann, M. Luchtenburg, B. R. Noack, R. King, M. Morzyński, and G. Tadmor, "Wake stabilization using POD Galerkin models with interpolated modes," in *Proceedings of the 44th IEEE Conference on Decision and Control, 2005 and 2005 European Control Conference (CDC-ECC'05)* (IEEE, 2005), pp. 500–505.
- ¹⁸ L. Lignarolo, D. Ragni, C. S. Ferreira, and G. van Bussel, "Turbulent mixing in wind turbine and actuator disc wakes: Experiments and POD analysis," AIAA Paper 2015-0223, 2015.
- ¹⁹ J. L. Lumley, "The Structure of Inhomogeneous Turbulent Flows," in *Atmos. Turbul. Radio Wave Propag.*, edited by A. M. Yaglom and V. I. Tatarski (Courier Corp., 2007), pp. 166–178.
- ²⁰ J. Meyers and C. Meneveau, "Optimal turbine spacing in fully developed wind-farm boundary layers," *Wind Energy* **15**, 305–317 (2012).
- ²¹ B. R. Noack, K. Afanasiev, M. Morzynski, G. Tadmor, and F. Thiele, "A hierarchy of low-dimensional models for the transient and post-transient cylinder wake," *J. Fluid Mech.* **497**, 335–363 (2003).
- ²² A. K. Prasad, "Stereoscopic particle image velocimetry," *Exp. Fluids* **29**(2), 103–116 (2000).
- ²³ S. Siegel, K. Cohen, J. Seidel, and T. McLaughlin, "Short time proper orthogonal decomposition for state estimation of transient flow fields," AIAA Paper 2005-296, 2005.
- ²⁴ S. Siegel, K. Cohen, J. Seidel, and T. McLaughlin, "State estimation of transient flow fields using double proper orthogonal decomposition (DPOD)," in *Active Flow Control* (Springer, 2007), pp. 105–118.
- ²⁵ S. Siegel, J. Seidel, C. Fagley, D. M. Luchtenburg, K. Cohen, and T. McLaughlin, "Low-dimensional modelling of a transient cylinder wake using double proper orthogonal decomposition," *J. Fluid Mech.* **610**, 1–42 (2008).
- ²⁶ L. Sirovich, "Turbulence and the dynamics of coherent structures," *Q. Appl. Math.* **45**, 561–571 (1987).
- ²⁷ J. N. Sørensen, R. Mikkelsen, D. S. Henningson, S. Ivanell, S. Sarmast, and S. J. Andersen, "Simulation of wind turbine wakes using the actuator line technique," *Philos. Trans. R. Soc., A* **373**(2035), 20140071 (2015).
- ²⁸ M. Tutkun, P. B. V. Johansson, and W. K. George, "Three-component vectorial proper orthogonal decomposition of axisymmetric wake behind a disk," *AIAA J.* **46**(5), 1118–1134 (2008).
- ²⁹ C. VerHulst and C. Meneveau, "Large eddy simulation study of the kinetic energy entrainment by energetic turbulent flow structures in large wind farms," *Phys. Fluids* **26**(2), 025113 (2014).